# An investigation into reach scale estimates of sub-pixel fluvial grain size from hyperspatial imagery

---

Martin Black

March 2013

Submitted for the degree of Master of Science by Research (MScR) in Physical Geography at the University of Durham.

# Declaration and Statement of Copyright

I confirm that no part of the material presented in this thesis has previously been submitted by me or any other person for a degree in this or any other university. In all cases, where it is relevant, material from the work of others has been acknowledged.



Martin Black
March 2013

# Acknowledgements

Firstly I would like to thank my lead supervisor, Dr. Patrice Carbonneau for his invaluable help and support throughout the year. I would also like to extend my thanks to my external supervisor Professor Michael Church (UBC) for providing funds to support a full field campaign, as well as his generosity and hospitality during my stay in Canada. His knowledge and expertise led valuable discussions throughout the course of the research. I would also like to thank my supervisor Dr. Jeff Warburton for his insightful opinions as well as comments on earlier revisions of this manuscript.

Special thanks goes to Dave Reid and Matt Chernos (UBC) for their support and help collecting field data, and for assisting with the collection of additional samples as required. I would also like to thank my family and friends for their support and guidance, and invaluable proof-reading and comments on earlier manuscripts.

# Abstract

Grain size data for gravel bed rivers is important in a wide variety of contexts; providing crucial information to guide the development of flood defences, and maintaining navigability, biodiversity and ecological integrity within large gravel bed rivers. Advances in remote sensing technologies have seen an increase in the acquisition of hyperspatial imagery (imagery with a spatial resolution of < 10 cm), and advances in computational power have complemented this data acquisition allowing for the application of complex image processing techniques. An improved methodology is presented for extracting reach scale grain size information. Of particular note is the ability to generate estimates of sub-pixel surface sand content, as well as sub-pixel grain size distributions. The methodology was applied to Queens Bar, N Bar, Calamity Bar and Harrison Bar within the gravel reach of the Fraser River (British Columbia, Canada).

Hyperspatial imagery was acquired at 3 cm resolution, along with independent surface grain size information. Surface sand estimates were calculated through a first order standard deviation textural layer; calibrations revealed an inequality based relationship between texture and sand content, allowing for the production of binary maps of surface sand content with an approximate accuracy of 70%. Calibrations were calculated for 7 grain size percentiles for the gravel fraction of the grain size distribution ( > 2 mm); $D_5$, $D_{16}$, $D_{35}$, $D_{50}$, $D_{65}$, $D_{84}$ and $D_{95}$ were achieved, following a wide ranging parameter investigation. A combination of first order standard deviation along with several second order Grey Level Co-occurrence Matrix textural parameters (entropy, contrast and correlation) calibrated to grain size using multiple linear regression. The best performing calibrations were found for smaller and intermediate percentiles; cross validated mean square error (%) at 0.61, 3.55, 9.58 and 16.25 for $D_5$, $D_{16}$, $D_{35}$, and $D_{50}$ respectively. Calibrations began to break down for the largest percentiles; cross validated mean square error (%) at 26.43 and 44.99 for $D_{84}$ and $D_{95}$. The breakdown of calibrations for larger percentiles is attributed to the 'pixel averaging effect'; for smaller percentiles a larger population of grains were averaged into one pixel, thus variance across multiple pixels is low, whereas for the larger percentiles the grain size approaches the spatial resolution of the pixels, therefore a smaller population of grains makes up one pixel and introduces increased variance across multiple pixels. Overall, this new methodology presents a means for extracting sub-pixel grain size information from hyperspatial imagery, with higher accuracies for the smaller percentiles than previously published. This allows for the rapid acquisition of a large amount of grain size information without the need for time intensive field techniques.

# Contents

# List of Tables



# List of Figures

# 1 Introduction

The Fraser River (British Columbia, Canada) drains a total area of 230,000 km$^2$ and is home to 2.5 million people (Census, 2001). In the lower reaches, the Fraser flows through agricultural and urban areas, and its sediments are of great importance. In recent times, pressure from land-use activities has placed fluvial economic, social and ecological functions at risk (Sparks, 1995; Gore and Shields, 1995; Rempel, 2004). Accurate sediment budgets provide crucial information to guide the development of flood defences, maintain navigability and the vast biodiversity and ecological integrity within the river (Gore and Shields, 1995; Ham, 2005; Rosenau and Angelo, 2007). Whilst information on the sediment budget is available (e.g. Ham and Church, 2003), current estimates of sediment transport could be improved significantly with data pertaining to the quantity of sand stored in the river bed (Ham, 2005; Church, *personal comm.*). Hence there is a need to address this uncertainty, specifically in reference to the finer grained fractions of the sediment budget.

> *...accurate quantification of the actual magnitude of sand and gravel volumes that enter, and are transferred through the reach over time, has proven difficult despite a considerable effort to establish these values.*
>
> Ham, 2005, p. 186.

Field based techniques to generate sediment budgets are time consuming and expensive; recent developments in fluvial remote sensing along with the increased availability of hyperspatial imagery (Rango *et al*., 2009; Carbonneau and Piégay, 2012) may provide a solution to this problem. Existing methods (Carbonneau *et al*., 2004, 2005) allow for the production of grain size maps limited to the coarse fraction of the grain size distribution. However, preliminary results presented by Chandler *et al*. (2004) suggest that the limited spectral information present in standard colour imagery is sufficient for the detection sub-pixel grain size information. Furthermore, anecdotal observations by Carbonneau (*personal comm.*) suggest that current methods of grain size mapping are in fact capable of detecting finer grains. Therefore, there is scope to push the boundaries of current methods and investigate their applicability for detecting surface sand content, which could provide crucial information on the sedimentary dynamics of large river systems.

Within remote sensing literature there are two main categories of techniques for extracting grain size information from digital imagery, close range photosieving techniques and reach scale techniques; the latter is of particular interest to this study. Current techniques using hyperspatial imagery have not exploited sub-pixel grain size information (where the grain size is smaller than the pixel resolution); methods have been limited to coarser grains, or used higher resolution imagery such that grains of interest occupy several pixels (e.g. Carbonneau *et al*., 2004, 2005; Verdú *et al*., 2005). Consequently, this study aims to extract sub-pixel grain size information, in terms of both sand and gravel. In conjunction with this study, on-going work at the University of British Columbia by Michael Church and colleagues aims to produce a probability distribution of sand depth measures; this

data will be combined with surface sand information to produce sand volume estimates within the Fraser. Overall this will reduce the need for time-intensive field mapping techniques which have proved difficult to apply to large river reaches, as well as providing crucial information for increasing the accuracy of sediment budgets.

# 2 Literature Review

## 2.1 A new sub-discipline; High Resolution Remote Sensing of Rivers

Rivers should be viewed as continuous systems; wherein features (e.g. water depth, sediment size, discharge) vary along the length and scale of the entire watershed of the river (Marcus and Fonstad, 2008). The majority of research into fluvial systems (geomorphology, hydrology, biology etc.) is derived from field studies which are often limited in terms of resolution (e.g. spatial or temporal), and these existing techniques do not provide centimetric resolution data at a watershed scale (Marcus and Fonstad, 2008). Recent technological advances in both remote sensing and computational power have led to the development of a new sub-discipline; high resolution remote sensing of rivers (Marcus and Fonstad, 2010). These technological advances are changing the way river scientists map, manage and analyse rivers; enabled through the use of remotely sensed data (Marcus and Fonstad, 2010). Of particular interest to this study is the acquisition of centimetre scale, hyperspatial imagery, and the subsequent development of image processing techniques to exploit information contained in hyperspatial images. Using hyperspatial imagery it has been possible to produce continuous watershed scale maps of various riverine features (including habitats, water depth, and grain size, amongst others), from sub-meter to centimetre resolution (e.g. Dugdale *et al*., 2010; Visser and Wallis, 2010; Hill *et al*., 2008 for a comprehensive review see Marcus and Fonstad, 2008).

Producing watershed scale maps is advantageous for river scientists as they can provide improved resolution as well as continuous data for the entire watershed rather than a limited reach (Marcus and Fonstad, 2008). Another major advantage achieved through the use of hyperspatial imagery is that techniques developed for extracting specific features may be transferred to other rivers, thus providing a wealth of data for multiple sites (e.g. Achar *et al*., 2011; Ierodiaconou *et al*., 2005). The development of automated and transferable techniques to exploit hyperspatial imagery will inevitably lead to a reduction in the need for time intensive and costly field mapping techniques whilst providing data for a range of applications and with consistently high accuracies (Marcus and Fonstad, 2010).

It must be stressed that within this new sub-discipline, techniques and algorithms that are being developed are still in their infancy (Marcus and Fonstad, 2010). Therefore there is scope to expand current methods and develop a technique which could provide crucial information on the sedimentary dynamics of large river systems. Before considering the current literature on remote sensing techniques for grain size mapping a brief review of image processing theory and background follows, introducing the concepts of block processing and image texture which are of particular relevance.

## 2.2 Digital Image Processing: Background

When processing hyperspatial digital imagery, it is important to define what is meant by a digital image, and by digital image processing. These are important concepts to consider as a prerequisite to understanding how image texture is calculated. In this context, we can define a digital image as the discrete function $f(x, y)$, where $x$ and $y$ are spatial coordinates and the amplitude of $f$ at any pair of coordinates is known as the grey level, or intensity (González and Woods, 2008).

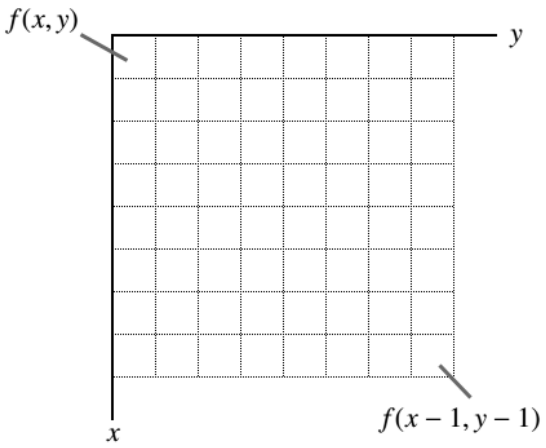


**Figure 1:** *Representation of a digital image in terms of* $f(x, y)$.

A digital image is composed of a finite number of elements, each having a particular location and value; these elements are also known as picture elements or more commonly pixels (González and Woods, 2008). This idea of digital images is visualised in Figure 1. Digital image processing thereby refers to the processing of these images by a digital computer (González and Woods, 2008). Another important aspect to consider is that of resolution. Perhaps most relevant to this study is the notion of spatial resolution, referring to the actual size of a pixel on the ground. This is usually quoted as a linear unit, with the assumption that pixels are square (Carbonneau and Piégay, 2012). Similarly, there are the concepts of spectral, radiometric and temporal resolution; spectral refers to the width of the spectral bands (such as Red, Green, Blue etc.) usually quoted in linear wavelength units such as nm, radiometric referring to the recording of information in a digital sensor (i.e. the amount of digital numbers stored for one pixel) usually quoted in bits, with 8-bit ($2^8$ or 256 possible values for one pixel) being most common, and temporal referring to the time between repeated imagery (Carbonneau and Piégay, 2012). The idea of sub-pixel information is also important to understand; extraction of sub-pixel information refers to the ability to discern properties which are smaller than the spatial resolution, and as such are entirely contained within one pixel (e.g. a 10 mm grain may be contained with one pixel at a spatial resolution of 30 mm).

Digital images and digital image processing techniques are used in a wide variety of disciplines; though perhaps most extensively in disciplines such as medicine (Pu *et al*., 2011; Deserno, 2011), and remote sensing (Lillesand *et al*., 2008; Sabins, 2007). There is also a wealth of literature within the field of computer science in relation to the development of theoretical concepts as well as the generation of algorithms and image processing techniques (Qidwai and Chen, 2009; González and Woods, 2008; Jensen, 2005; González *et al*., 2004).

Image texture techniques will be applied to the digital imagery used in this study; specifically, the Grey Level Co-occurrence Matrix (Haralick, 1979). The Grey Level Co-occurrence Matrix (GLCM) has been investigated by others and is known to produce calibrations between image texture and grain size information (e.g. Verdú *et al*., 2005; Carbonneau *et al*., 2004). However, the GLCM has a wide variety of input parameters and is relevantly complex to compute. Therefore there is scope to investigate the parameter space of the GLCM and its relationship to grain size; only a limited parameter space was investigated by Verdú *et al*. (2005) and Carbonneau *et al*. (2004).

### 2.2.1 Block Processing

An important concept which is often used for calculating image texture measures, is that of *block processing operations*. These involve the use of a window, or kernel, and can be generalised as shown in Equation 1

$$g(x, y) = T[(f(x, y)] \tag{1}$$

where $f(x, y)$ is the input image, $g(x, y)$ is the output image, and $T$ is an operator on $f$ defined over a neighbourhood of point $(x, y)$ (González and Woods, 2008). The operation, $T$ is applied in a neighbourhood centred on the point $(x, y)$ and the new image, $g$, is created by sliding the window so that $T$ is applied at all blocks of image $f$ (González and Woods, 2008). This idea of block processing operations can be visualised in Figure 2.

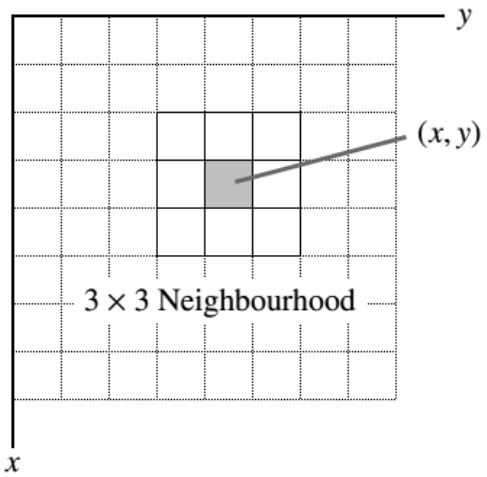


**Figure 2:** *An example of a* 3×3 *block processing operation. The neighbourhood would be moved across by* 3 × 3 *pixels across the whole image to generate a new output image (Adapted from González and Woods, 2008).*

Generally, square windows (e.g. 3 × 3, 5×5, 7×7 and so on) are preferred due to their unambiguous centre point, though this method applies to windows of any shape or size. Special consideration must be made when the operator $T$ is applied to areas on the edges of the image $f$. In such areas, the window may not be entirely enclosed within the pixels of the original image, leading to *edge effects*. These effects can be alleviated by 'padding' the original image This involves adding new values (e.g. zeroes) around all sides of image $f$ by half of the window size, such that the size of image $f$ becomes $(m + (w + 1/2)) \times (n + (v + 1/2))$, where $m$ and $n$ are the rows and columns of image $f$ and $w$ and $v$ are the size of the kernel. Image texture is calculated through block processing of digital images.

### 2.2.2 Image Texture and The Grey Level Co-occurrence Matrix

Image texture analysis involves quantifying the texture content of an image; it is directly calculated by assessing the differences in brightness values between neighbouring pixels. Generally large differences in brightness values between neighbouring pixels results in high texture, whereas smaller or no difference in brightness values equates to low texture. Texture layers can aid in the classification process as they provide additional information to help identify regions within an image (e.g. Clausi, 2002). Texture operations can be split into two types; first and second order (Hall-Beyer, 2007). First order methods are calculated directly from the original image pixels and are often simple statistical measures; pixel neighbour relations are not considered (Hall-Beyer, 2007). Some common measures of first order texture include mean, standard deviation (and variance), range and entropy.

The Grey Level Co-occurrence Matrix (GLCM) (Haralick *et al.*, 1973) is an example of a second order texture measure; unlike first order measures the GLCM considers the spatial relationship of the pixels, whereas first order measures do not (Hall-Beyer, 2007). Following the example outlined by González and Woods (2008), a GLCM can be defined as follows: let $O$ be an operator that defines the spatial relationship of two pixels relative to each other, and an image $f(x, y)$ with $L$ possible intensity levels. The GLCM, $\mathbf{G}$, is a matrix whose element $g_{i,j}$ is the number of times that pixel pairs with intensity levels $z_i$ and $z_j$ occur in the image, $f$ at the position specified by $O$. Figure 3 shows an example for image $f$ where $L = 8$, and $O$ is defined as "one pixel to the right". We can see in the example that element $(6, 2)$ of $\mathbf{G}$ has a value of 3, as there are 3 occurrences in image $f$ of a pixel value of 6 where its neighbour to the immediate right $(0, 1)$ has a value of 2.

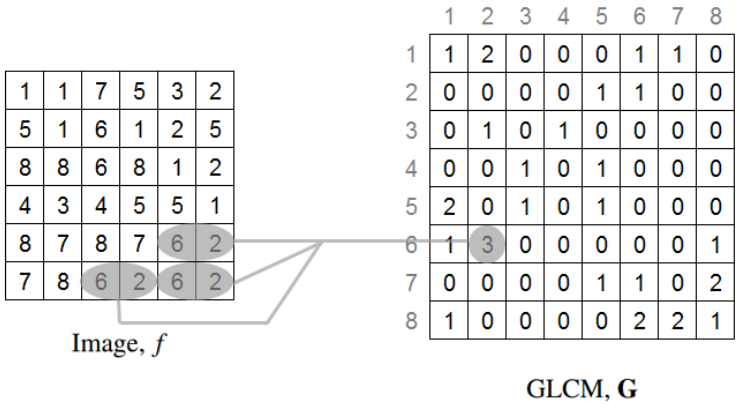


**Figure 3:** *An example of calculating a Grey Level Co-occurrence Matrix (Adapted from González and Woods, 2008).*

| Feature | Formula | |
|---|---|---|
| Autocorrelation | $\sum_i \sum_j (ij) p_{ij}$ | (2) |
| Contrast | $\sum_i \sum_j (i-j)^2 p_{ij}$ | (3) |
| Correlation | $\frac{\sum_i \sum_j (i,j)\ p(i,j) - \mu_x \mu_y}{\sigma_x \sigma_y}$ | (4) |
| Dissimilarity | $\sum_i \sum_j \mid i-j \mid \cdot p_{ij}$ | (5) |
| Energy *or* Angular Second Moment | $\sum_i \sum_j (i-j)^2$ | (6) |
| Entropy | $-\sum_i \sum_j p_{ij} log(p_{ij})$ | (7) |
| Homogeneity *or* Inverse Difference Moment | $-\sum_i \sum_j \frac{p_{ij}}{1+ \mid i-j \mid}$ | (8) |
| Maximum Probability | $max_{ij}(p_{ij})$ | (9) |

**Table 1:** *Equations for calculating GLCM Features (after Haralick, 1979; Haralick* et al.*, 1973), compiled from González and Woods (2008) and Soh and Tsatsoulis (1999).*

Following the generation of a GLCM it is necessary to normalize it. Equation 10 is the equation used to transform the GLCM into a close approximation of a probability table; this however is only an approximation because a true probability would require continuous values whereas the grey levels have been discretized (Hall-Beyer, 2007).

$$p_{ij} = \frac{V_{ij}}{\sum_{ij=0}^{N-1} V_{ij}} \tag{10}$$

where $V$ is the GLCM value at the point $i$, $j$ and $P$ is the normalised GLCM value at the point $i$, $j$.

Several GLCM features can also be calculated, as shown in Table 1. These features were suggested by Haralick (1979) and Haralick *et al*. (1973). The equations shown are compiled from González and Woods (2008) and Soh and Tsatsoulis (1999). It is worth noting that equation 4 has been proven to be identical to semivariance, and gives nearly identical results to autocorrelation methods using Moran's I or Geary's C (Van Der Sanden and Hoekman, 2005; Hall-Beyer, 2007). The GLCM and its related statistics are calculated using a block processing method as described above; the returned statistic is added to the point $g(x, y)$ in the new output image.

## 2.3 Data Sources for Grain Size Mapping

Watershed scale information pertaining to surface grain size variability in gravel bed rivers such as the Fraser, is crucial for understanding and explaining sediment transfer processes and is important in many contexts, such as geomorphology, ecology and engineering (Graham *et al*., 2010; Carbonneau *et al*., 2005). The developments of digital image processing techniques and their application in this new sub-discipline enabled through the acquisition of hyperspatial imagery have led to improvements in the application of non-invasive techniques to provide grain size information at a quality comparable to that of traditional field techniques (Graham *et al*., 2010).

As hyperspatial imagery is the main dataset to be used, the exploitation of spatial and spectral information from optical colour imagery is the primary focus of this research. As well as this, optical imagery is often widely available through both private and public sector agencies and commercial vendors; many holding archives of high resolution data which could be exploited for change detection (Marcus and Fonstad, 2008). Increasingly, researchers and agencies are moving toward collecting their own imagery using off-the-shelf cameras and various imaging techniques such as platforms, balloons, Unmanned Aerial Vehicles (UAVs), and private aircraft (Marcus and Fonstad, 2008). Hence a focus on developing a technique applicable to this imagery would be very beneficial and through exploitation of archival imagery, could lead to a wealth of information for both modern and historical data collection and analysis. As well as this, the advantages of using a non-invasive and automated technique allows for rapid data collection and analysis at a much higher spatial and temporal resolution than is possible with standard field techniques (Graham *et al*., 2010). Therefore, the following section explores digital image processing techniques used by others for extracting grain size information from digital images.

## 2.4 Estimating Grain Size from Ground based Digital Imagery

The techniques for measuring surface grain size information in the field are well established (mainly following Wolman, 1954). The most commonly applied technique for calculating surface grain size variability is the grid-by-number technique, where grains are blindly selected from the surface in a grid pattern (Green, 2003; for a full description of the technique see Leopold, 1970). An investigation into the errors associated with grain size percentiles calculated from a grid-by-number technique by Rice and Church (1996) found that percentile precision improved with increasing number of samples, as would be expected by statistical theory. To achieve 95% confidence intervals of $\pm 0.1\psi$ ($\psi = -\phi = log_2\ mm$), a sample size of 400 stones is required (Rice and Church, 1996). The spatial variability of fluvial sediments over a variety of scales means that considerable effort is required in the field to characterise these sediments (Church *et al*., 1987). Even techniques such as grid-by-number may not give the required precision - for example, a large cell size may cover a variety of different grain sizes, thereby leading to an imprecise

estimate of grain size parameter(s) (Graham *et al*., 2005a).

The development of image-based techniques for collecting grain size data in the field presents numerous advantages over time-intensive field techniques, such as those described above. The advent of photosieving based field techniques (Ibbeken and Schleyer, 1986) reduced the need for surface sampling and increased the resolution at which data could be collected; images could be rapidly acquired in the field and grains manually measured from the image at later date. More recently, automated procedures to extract grain size information from digital images have been well developed. Initial studies used small sample sizes and a small number of images under controlled laboratory conditions (McEwan *et al*., 2000; Butler *et al*., 2001). The methodology developed by Graham *et al*. (2005a; 2005b) represented the first major development of a transferable method for measuring grain size information from *in situ* images of sediment. Several permutations of image segmentation techniques were applied on a dataset of 39 images, with the optimum technique using a combination of a morphological bottom-hat transform with a double threshold (Graham *et al*., 2005a). Testing of the image segmentation procedures on a dataset comprised of various lithologies, shape, texture and roundness from different rivers resulted in an area-by-number percentile error of less than 0.05 $\psi$ (Graham *et al*., 2005b). Whilst percentile errors are low, the grain size distributions are truncated; the segmentation of individual grains breaks down for smaller particles, thus grains smaller than 16 mm (23 pixels) are truncated from the distribution (Graham *et al*., 2005a). Hence derived distributions may not be completely representative of those on the ground; the removal of the finer grains may significantly influence the overall shape of the grain size distribution as well as calculation of the percentiles.

Rubin (2004) present a methodology using autocorrelation lags to calculate grain size. Autocorrelation curves are calculated (see Rubin, 2004 for a working example in MATLAB), and calibrated to grain size curves calculated by traditional sieving of sediment. Autocorrelation curves from images of sediment can then be computed and the proportions of each grain size fraction can be calculated, using a least squares fit with the calibrated curve. The correlation between traditional sieving and the autocorrelation technique is reported with an $R^2$ of 0.966 (Rubin, 2004). This technique has also been subsequently developed by Warrick *et al*. (2009). Warrick *et al*. (2009) worked on images with an approximate spatial resolution of 0.3mm, and tested the applicability of the autocorrelation technique (Rubin, 2004) to generate grain size maps for predominantly coarse grained environments such as mixed beaches and gravel bars (Warrick *et al*., 2009). Results show RMS values of 14% for images taken with ambient lighting. Warrick *et al*. (2009) however note that their technique may be impractical for evaluating grain size patterns at reach scale. As well as this, the applicability of this method for assessing the finer grained fractions is not considered (Warrick *et al*., 2009).

Buscombe *et al*. (2010) present an approach to measure the mean grain size from an image, without the need for complex image analysis techniques or calibration from field data. Following from the methods outlined by Rubin (2004), autocorrelation techniques

were used, however, they were applied in the frequency rather than the spatial domain, using a two-dimensional autocorrelation function (Buscombe *et al*., 2010; Buscombe, 2008). The technique suggested by Buscombe (2008) allows an estimate of major and minor grain diameters, therefore suggesting that mean grain size can potentially be determined without calibration. Buscombe *et al*. (2010) subsequently extended this methodology and developed an approach for calculating mean grain size. Following validation the technique was found to have an RMS of 16%. Whilst the results of this study are a promising evolution from the original autocorrelation methods suggested by Rubin (2004), their application was to images of sediment where the spatial resolution was ~0.5 mm (or smaller), hence this technique will not be directly applicable at reach scale as entire grains occupy several pixels.

More recently, in a series of papers, Buscombe and Rubin (2012a; 2012b) present techniques for the calculation of the geometric properties of granular material from digital imagery. A similar application of the Fourier (frequency) spectrum techniques presented in Buscombe *et al*. (2010) was applied, with the extension of measuring particles with a significant void fraction (i.e. particles which are not touching) (Buscombe and Rubin, 2012b). The new method uses an autocorrelogram of the sediment image estimated through a Fourier transform, as well as a modelled autocorrelogram with the same particle size, but zero variance (a uniform distribution). From this, statistical methods are used to estimate the arithmetic sorting coefficient for sediment with and without a void fraction. A modification of the algorithm presented in Buscombe *et al*. (2010) for calculating mean particle size is also proposed for sections with known void fractions. The methods presented also have no tunable parameters or empirically derived coefficients, meaning they should have broad applicability (Buscombe and Rubin, 2012b).

An alternative technique is presented by Pina *et al*. (2011), based mainly on mathematical morphology operations (Serra, 1982), such as erosion and dilation, to directly compute a complete grain size distribution curve from images captured in the field, with results comparable to those obtained by sieving (Pina *et al*., 2011). Their approach involves successive morphological operations of erosion followed by dilation, increasing in size, on a grey scale image of sedimentary grains (Pina *et al*., 2011). They used a square structural element to provide a comparison with traditional sieving processes. With each iteration of the morphological operator (with the structural element increasing in size), darker objects within the greyscale image were progressively eliminated and a curve of the sum of the grey levels is computed (Pina *et al*., 2011). A max tree approach was used in order to produce a more efficient computation. Results indicated a Mean Square Error (MSE) of 0.105 $\psi$ (for $D_{50}$) when validated against traditional sieving techniques. However, the imagery used in this study had a spatial resolution of 0.014mm, with even the smallest sand grain represented by at least $4 \times 4$ pixels.

Chang and Chung (2012) present a methodology combining image processing techniques similar to Graham *et al*. (2005a), along with a feedback pulse couple artificial neural network and multilevel thresholding (e.g. Xue and Yang, 2005) to automatically extract grain

size information from digital images of river sediment. Their technique also proposes a decisive image-merging algorithm to improve the quality of image segmentation results. Similar to Graham *et al*. (2005a), the measurement and derivation of grain size characteristics hinges on the accurate segmentation of a digital image into its constituent grains - the more precisely these grains can be segmented in a digital image, the more precise estimates of grain size information will be (Chang and Chung, 2012). The methodology was developed and applied to lab and field data, and compared to existing techniques as well as manual sieving. Results indicated average Root Mean Square Error (RMSE) of $0.1\psi$ in the lab and $0.2\psi$ in the field (Chang and Chung, 2012). Their results consistently provided more precise estimates of grain size distributions and calculation of specific percentiles, compared to the methods of Graham *et al*. (2005a,b) and Xue and Yang (2005). Whilst their method is found to be consistently more precise, they also truncated distributions to provide a fairer result (Chang and Chung, 2012); accuracy assessment of distributions is based on a 16 mm truncation, however their calibrations do produce good estimates of grain size, even for the finer grained fraction (< 16 mm) (Chang and Chung, 2012).

## 2.5 Estimating Grain Size from Reach-scale Digital Imagery

One of the major approaches for extracting grain size information, especially relevant to this study, is using the textural characteristics of digital imagery to extract grain size information. Carbonneau *et al*. (2004) considered measures of image texture and two-dimensional semivariance to estimate grain size using both 3 cm and 10 cm aerial imagery. Photosieving techniques were used to calculate ground truth grain size data from a midchannel bar; this bar was selected as a pilot study site as it contained the full range of grain sizes (Carbonneau *et al*., 2004). Images were initially segmented to leave the dry gravel bed area only, using the intensity band of a hue-saturation-intensity (HSI) image and Otsu's method of histogram segmentation (Otsu, 1979). The images were also corrected specifically for both methods of texture and semivariance. For image texture, the brightness was normalised between images to correct for illumination changes and for semivariance a histogram shift was applied to give dry gravel patches an equal mean brightness of 150 (Carbonneau *et al*., 2004). Both measures were calculated in local windows on the image, with a range of window sizes from $5 \times 5$ to $50 \times 50$ pixels (px), generating 20 grain sizes images. For each of these 20 images, the *b* axis of the groundtruthed images (obtained through photosieving) was plotted against the calculated image properties (semivariance and texture) to produce a relationship which could subsequently be used to estimate grain size (Carbonneau *et al*., 2004). The predictive relationships calculated using image properties and grain sizes were validated using independent data collected through manual sampling.

Whilst image texture measures had potential, they failed at the validation stage; the most promising technique proved to be image semivariance at a window size $33 \times 33 px$ (Carbonneau *et al*., 2004). Following validation with the independent field data, the predictive

relationship was found to have an $R^2$ of 0.96, and an overall precision of ±15.4% for estimating $D_{50}$ (Carbonneau *et al*., 2004). Six key parameters were identified for producing reliable grain size maps: window size, image resolution (ground footprint), scale of ground truth data, scale of uniform gravel patches, median particle size ($D_{50}$) and number of pixels required for a semivariogram sill to be present (Carbonneau *et al*., 2004). Perhaps the most important of these parameters is the presence of a semivariogram sill, as grain size is calculated from the sill value. The semivariogram sill is the lag at which maximum semivariance is reached. As particles get coarser there is an increased probability they will cover more homogeneous zones of light or dark, hence the brightness values of the image will reflect this, therefore a correlation between grain size and sill value can be made (Carbonneau *et al*., 2004). Hence the window size must be big enough to have the presence of a sill in the calculated semivariogram. A key point to note is that the $D_{50}$ values calculated were greater than the spatial resolution of the imagery used, with no investigations of the finer, sub-pixel grain size calibrations.

Similarly, Verdú *et al*. (2005) investigated several methods of image texture analysis (including the semivariogram approach) for mapping grain size at reach scale. Using two sets of imagery at scales 1:1000 and 1:40, texture measures were used to calculate grain size percentiles. On the 1:1000 scale imagery, five different texture measures were calculated using a Grey Level Co-occurrence Matrix (GLCM); variance, homogeneity, contrast, entropy and second angular moment (Verdú *et al*., 2005; Haralick *et al*., 1973). Following initial testing on 10 random test bars the mean and standard deviation of the *variance* and *contrast* GLCMs in a $7 \times 7$ window with shifts of $(-3, +3)$ and $(+3, +3)$ were selected for further investigation along with the mean and standard deviation of local pixel values in a $7 \times 7$ window (Verdú *et al*., 2005). As well as the GLCM methods, semivariance values with distances up to 12 pixels were calculated and used as texture measures; the semivariogram texture method was calculated on 1:40 and 1:1000 scale imagery. The combination of these scales gave semivariance texture measures at distances of 6 to 72cm (from the 1:1000 scale imagery) and 0.3 to 3.6cm (from the 1:40 scale imagery) (Verdú *et al*., 2005). This meant that there were 33 values of texture; 9 GLCM measures and 24 semivariance measures (Verdú *et al*., 2005). Multiple Linear Regression was used to calculate equations for estimating grain sizes; this process was cross validated by retaining 25% of the bars for validation and using repeated iterations until all bars had been used for both regression and validation (Verdú *et al*., 2005). Using these equations, grain size maps were created using orthophotos of the bars, and vegetated and flooded pixels were masked; the test bars used had facies which represented the whole reach, and a constant sun angle during image acquisition meant that the equations generated could be applied to the whole reach (Verdú *et al*., 2005). Using regression, several different texture variables were selected for mapping grain size percentiles, from $D_{10}$ to $D_{90}$ (see Table 3, Verdú *et al*., 2005, p.86). Using simplified equations, due to computational constraints, $R^2$ values of up to 0.86 could be achieved, with error estimation being lower for intermediate percentiles (e.g. $D_{50}$ with an RMS of 18%) (Verdú *et al*., 2005). Again, similarly to Carbonneau *et al*. (2004), sub-pixel grain size information was not addressed; multiple linear

regression with both scales of imagery provided calibration with the finer percentiles. The 1:40 scale imagery, with a spatial resolution of 3 mm was an order of magnitude smaller than the lowest percentile ($D_{10}$ at 30 mm), meaning sub-pixel grain size information was not considered.

Preliminary work into reach scale measures of grain size information by Chandler *et al*. (2004) was carried out using a combination of simple image texture and image classification techniques. A combination of supervised image classification along with the calculation of a $3 \times 3$ pixel variance convolution filter was used. Classifications were found to have a 'true' accuracy of 49% using just RGB imagery (Chandler *et al*., 2004). Investigations into autocorrelation and semivariogram approaches yielded slight improvements, with accuracies of up to 51% achieved. Using 1:5000 scale imagery, overall classifications of standard RGB imagery and an additional texture layer were achieved at 56% accuracy, with a three-fold classification into sand, pebble and cobble. Investigations also revealed that changing between 1:5000 and 1:10,000 scale imagery did not greatly affect the resulting classification accuracy (Chandler *et al*., 2004). The authors highlight that further investigation into deriving sand content is required, with maximum accuracy for sand classification around 42% (Chandler *et al*., 2004). This work provides proof of concept to the idea that sub-pixel patterns of sand and gravel can be derived from images, with the addition of an image texture layer and use of image processing techniques.

## 2.6 Summary

Given this brief review of the available literature, there has been relatively limited exploration of image texture techniques for extracting sub-pixel grain size information, such as sand, gravel and other finer grained material. The work by Verdú *et al*. (2005) and Carbonneau *et al*. (2004) provides a basis for the exploration of image texture techniques and calibration with grain size information, whilst Chandler *et al*. (2004) provides a promising insight into the application of methods for providing reach scale grain size maps of sub-pixel grain size information, albeit with a somewhat low accuracy. The range of image texture parameters investigated in these studies is also somewhat limited, therefore there is plenty of scope for further research into these methods. The literature on digital image processing with reference to grain size characterisation is dominated by the ever evolving techniques related to close range imagery; imagery wherein entire grains are present. There has been relatively limited work on surface measures of grain size at reach scale. This study aims to further investigate the methods applied by Carbonneau *et al*. (2004) and Verdú *et al*. (2005) to investigate the applicability of image processing techniques for mapping the sub-pixel portions of the grain size distribution. Specifically within the Fraser, there is a known problem of quantifying sand and fine gravels within the sediment budget (Ham, 2005), therefore an image processing technique may address this problem. Consequently, aims and objectives for this study are outlined in Section 3.

# 3 Research Aim and Objectives

Following the background outlined in Sections 1 and 2, the main aim of this study is given below:

- To investigate the ability for image processing techniques using image texture parameters to produce a method capable of extracting sub-pixel grain size information from hyperspatial imagery, at reach scale.

Drawing from this aim, the following research objectives have been identified:

1. Produce a method capable of mapping surface sand content from hyperspatial imagery.
2. Investigate the feasibility of extracting a grain size distribution for the gravel fraction (i.e. greater than 2mm).

# 4 Methodology

Digital imagery of four large gravel bars was acquired at 3 cm spatial resolution, along with contemporary measures of surface grain size information through field and laboratory sieving, and photosieving. Ground level photographs and GPS data of homogeneous sand areas were also collected. The presence of sand was investigated through a simple first order texture measure, and assessed with comparison to manually delineated sand areas. Calibrations of grain size distribution for the gravel fraction were investigated using image texture via the GLCM (Haralick *et al*., 1973; Haralick, 1979), and an in depth range of parameters. Statistical techniques of regression (linear and multiple linear) were applied to calibrate image texture to grain size information, with the resulting calibrations assessed through leave-one-out cross validation. Following calibration with grain size information, optimal parameters were identified and grain size maps produced.

## 4.1 Study area: The Fraser River

The source of the Fraser lies within Mount Robson Provincial Park, British Columbia. It drains an approximate area of around 230,000km$^2$, which equates to around one quarter of the province (Rosenau and Angelo, 2007). Several tributaries contribute to the vast flows within the Fraser, including large streams such as the Quesnel, Chilcotin, Bridge and Thompson (Rosenau and Angelo, 2007). Following the terminology outlined in Rosenau and Angelo (2007), this study is concerned with a 100 km reach of the lower Fraser river from Hope to Mission, also termed the *gravel reach*, due to the predominant sediment

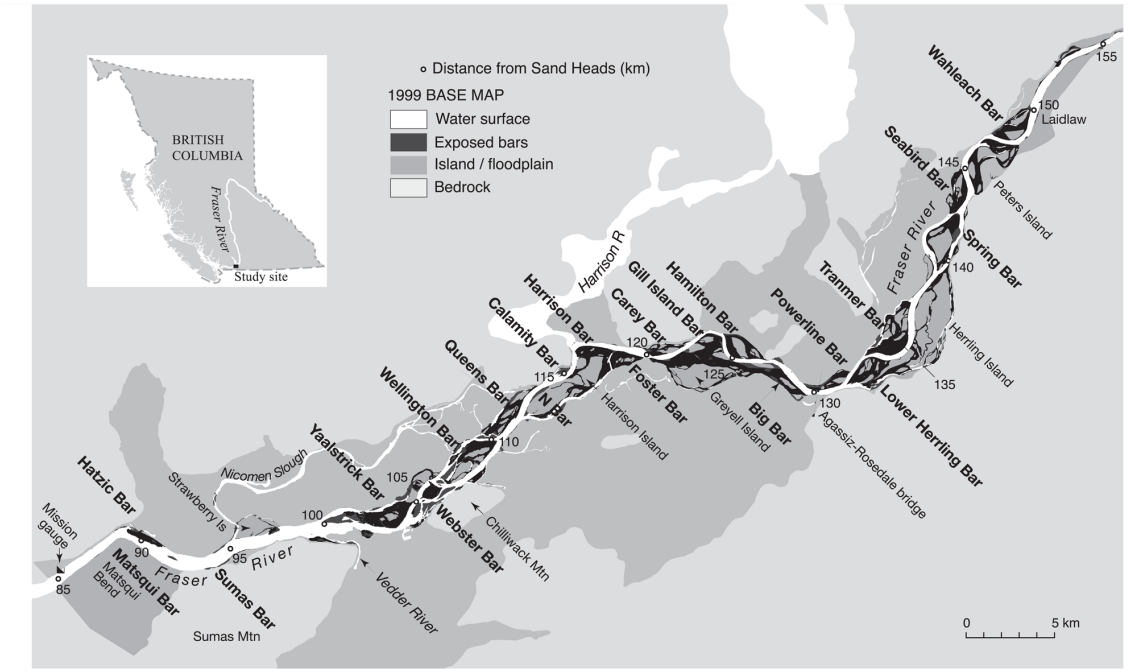


**Figure 4:** *Map showing the gravel reach of the Fraser River, between Laidlaw and Mission, British Columbia, Canada. River kilometres are measured from Sand Heads (mouth of the river); the major bars are named (from Rice and Church, 2010).*

type in this region (Rosenau and Angelo, 2007; see Figure 4). Specifically, the gravel bars photographed and of interest to the study are Queens Bar, N-Bar, Calamity Bar and Harrison Bar (see Figures 4 and 8).

In river reaches which have unconfined alluvial channels, such as the *gravel reach* of the Fraser, a complex channel system can form (Rosenau and Angelo, 2007). In the Fraser this includes features such as secondary channels, mid-channel bars, backwaters and islands (Rempel, 2004). These features support a diverse and productive ecosystem; a direct result of the physical habitats made available in the gravel reach (Rosenau and Angelo, 2007; Rempel, 2004). The following sections will discuss the hydrology (Section 4.1.1), geomorphology and ecosystems (Section 4.1.2) and sediments (Section 4.1.3) within the Fraser.

### 4.1.1 Hydrology of the Fraser River

The flow through the gravel reach of the Fraser is considered to be relatively stable throughout the year (Rosenau and Angelo, 2007). Mean monthly discharge collated from 1965 to 1992 at the Mission gauging station (Environment Canada, 2011) at the end of the gravel reach is shown in Figure 5. The maximum discharge occurs as a result of snow-melt due to warming spring temperatures; hence peak flow is achieved in June. In smaller tributaries the timing of the freshet is generally later (Rosenau and Angelo, 2007). This is a result of rainfall events in late autumn or early winter causing snow melt on snow packs which have accumulated in local watersheds; these rainfall events coupled with snow-melt can cause severe flooding; these tributaries therefore show a freshet in late autumn or early winter unlike the spring dominated freshet seen in the Fraser (Rosenau and Angelo, 2007).

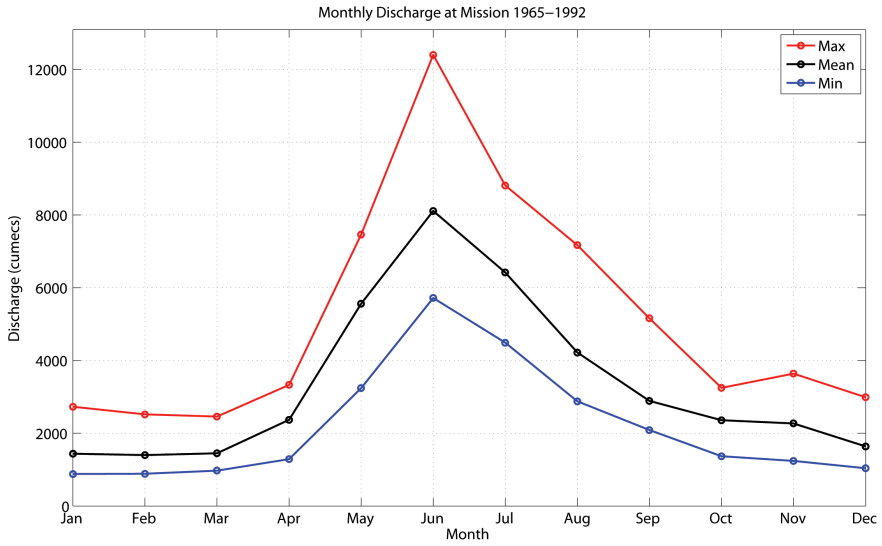


**Figure 5:** *Mean monthly discharge (1965-1992) at Mission (Environment Canada, 2011). Discharge is given in* $m^3/s$.

Winter discharge at Mission remains relatively stable at ~2000 $m^3/s$ with peak discharge occurring in June at ~8000 $m^3/s$ (and up to as much as 12000 $m^3/s$, e.g. June, 1972). The spring freshet strongly affects the riparian ecosystems in the Fraser due to a substantial increase in water surface elevations (Rosenau and Angelo, 2007). At Mission this equates to an average rise in water surface elevation of ~3.35m (from a minimum of ~0.93m in March to a maximum of ~4.3m in June) (Environment Canada, 2011). As a result of substantial flooding in 1948, the gravel reach has been extensively managed; approximately $ 300 million has been invested in flood defences, with ~600km of dikes now in place (Fraser Basin Council, 2008). The extensive dyking of the gravel reach prevents the lateral flow of nutrients, sediments and water onto the floodplain. This therefore inhibits the diverse ecosystems found both instream and in the riparian areas of the Fraser which are dependant on the hydraulic pathways provided by rising flood waters (Rosenau and Angelo, 2007).

### 4.1.2 Geomorphology and Ecology of the Fraser

The ecosystems maintained within the aquatic and riparian habitats of the Fraser are due to complex stream-bed patterns; these patterns are altered through the downstream movement of sediment, and the repositioning of the main 'deep' channel through erosion of sediments (in the channel) and deposition of sediments (on channel bars) (Rosenau and Angelo, 2007; Church, 1983). Ham (2005) suggests that in rivers such as the Fraser, a homogeneous reach is primarily influenced by both flow and sediment regimes and valley gradient. Other features such as bank strength, land use patterns, riparian vegetation and anthropogenic influences are important secondary factors which also influence the stream bed patterns (see Chapter 2 in Ham, 2005 and references therein).

The substantial power within the flow of the Fraser is what facilitates the morphological changes within the islands, channels and floodplain areas of the gravel reach, as a direct result sediment transfer (through erosion and deposition) (Rosenau and Angelo, 2007; Ham, 2005). It is this flow which works to continually renew the aquatic and riparian habitats and provides physical niches for organisms (Rosenau and Angelo, 2007). In the upper ~1000 km of the Fraser (from its headwaters), the channel configuration is single-threaded and confined, until it flows into the gravel reach (Rosenau and Angelo, 2007). In the area of the gravel reach, the Fraser is transformed from its single channel configuration into a pattern consisting of multiple irregular sinuous channels which split around large sand and gravel bars and island complexes as the gradient declines downstream (Rosenau and Angelo, 2007; Ham, 2005). This is known as a wandering or braided gravel bedded stream (Tockner *et al.*, 2006). The dynamic nature of braided rivers leads to a Shifting Habitat Mosaic (SHM), whereby the erosion and deposition of sediments, channel avulsion and other factors create a complex array of habitats (both aquatic and terrestrial) (Rosenau and Angelo, 2007, 2005; Tockner *et al.*, 2006).

As a result of the natural wandering gravel bed system described above, many of the side channels of the Fraser have become isolated from the main flow and naturally developed into wetlands; these wetlands provide habitats which support a diverse array of organisms (Rosenau and Angelo, 2007). Many of these areas have since been drained and used for agricultural purposes, or in some cases regularly flowing secondary channels have been isolated through the construction of barriers; some as recently as the early 1990s (Rosenau and Angelo, 2007). Studies (e.g. Rosenau and Angelo, 2007; Ellis *et al*., 2004; Rosenau and Angelo, 2000) have shown that there have been substantial decreases in bank length compared to historic records; for example Ellis *et al*. (2004) report that bank length has decreased by 44% since ~1900. The loss of the secondary channels subsequently has a high impact on their habitats, leading to a dramatic reduction in their capacity (Rosenau and Angelo, 2007).

Vegetated island complexes within the channels of the gravel reach of the Fraser, particularly those which are prone to flooding, are another area with a rich and diverse ecosystem (Rosenau and Angelo, 2007). These islands can be seen as important landscape elements; in many areas of the world they are colonised by a range of flora and fauna and can even provide a refuge for endangered species (Rosenau and Angelo, 2007; Tockner *et al*., 2006). They may also provide pathways to support the migration of small mammals, and are somewhat protected from invasive species due to their isolation within the channel (Rosenau and Angelo, 2007; Tockner *et al*., 2006). The modification of the channels, e.g. through the construction of barriers, directly influences the ecology of these island complexes; this has been especially widespread for large river systems in Europe, and acts to reduce the number of unmodified complexes available for ecological studies (Rosenau and Angelo, 2007; Tockner *et al*., 2006).

The gravel reach of the Fraser contains a greater diversity of fish species than any other freshwater ecosystem in British Columbia (Rosenau and Angelo, 2007). Within this reach there are large populations of Pacific Salmon, including pink (*Oncorhynchus gorbuscha*), chinook (*O. tshawytscha*), coho (*O. kisutch*), sockeye *(O. nerka*) and chum (*O. keta*) (Rosenau and Angelo, 2007). Pink salmon are known to spawn every other year within both the main channel and secondary channels which are free-flowing and connected to the main channel; the numbers of spawning fish regularly reaches several million due to the abundant gravel habitat which they occupy (Rosenau and Angelo, 2007). The decomposition of adult pink salmon bodies is known to contribute greatly to the aquatic ecosystems through the input of nitrogen and phosphorus; these are subsequently sequestered by aquatic algae and recycled to higher trophic levels once the algae is eaten (Rosenau and Angelo, 2007). Other fish species, such as the white sturgeon are also found within the Fraser. White sturgeon are the largest freshwater fish species found in North America; they can grow up to as large as 4m in length and weigh up to 450kg (Rosenau and Angelo, 2007). These fish are known to spawn in the gravels and cobbles in autumn and winter and in spring and summer they migrate downstream into areas of sands, another key habitat within the Fraser (Nelson *et al*., 2004). These species, in combination

with several others found in the Fraser (see chapter 2 in Rosenau and Angelo, 2007 for a comprehensive review) contribute to the vast biodiversity and range of both aquatic and riparian ecosystems, as well as having both economic and recreational values (Rosenau and Angelo, 2007; Scott and Crossman, 1985).

### 4.1.3 Sediments within the Fraser

Unsurprisingly, gravel is the predominant sediment type within the gravel reach of the Fraser. However, there is also an abundance of other sediment classes within the reach, sorted both horizontally and vertically within the channel system (Rosenau and Angelo, 2007). The sediments become increasingly finer downstream reflecting the decreased horizontal gradient and widening floodplain. Gravels and cobbles tend to dominate in the channel and bars upstream at Hope, but the sediment becomes progressively finer further downstream towards Mission where sand is the major component (Rosenau and Angelo, 2007).

The smaller sized alluvial sediments such as silts and sands comprise a relatively large fraction of the total sediments in the gravel reach, with sand playing a key role in the sediment budget of the Fraser (Rosenau and Angelo, 2007). Up to as much of 30% of bulk samples taken from mid-river bars can be composed of sand (Church *et al*., 2001) along with other finer grained sediments. Sand constitutes a substantial portion of the overbank areas (Rosenau and Angelo, 2007). Natural erosion processes between the early 1950s to mid 1980s resulted in significant losses of overbank sand from the gravel reach (Ham, 2005), however extensive protection of the banks in the 1970s may have acted to prevent this (Rosenau and Angelo, 2007). Whilst finer grained sediments such as sand usually play a small role in the net erosion / deposition volumes of the gravel reach, in some areas large volumes of sand, which make up the surface topography of some of the banks and islands, have been lost (Ham, 2005). This has acted to balance the volume of total sediment erosion / deposition (Rosenau and Angelo, 2007). Therefore, the total erosion and deposition of sediments can be seen to be in equilibrium (Rosenau and Angelo, 2007; Ham, 2005; Ham and Church, 2003).

The diversity of ecosystems and habitats found within the Fraser is dependent on the rich soils formed as a result of the deposition of finer grained sediments; these soils provide a basis for the natural vegetation communities within Fraser (Rosenau and Angelo, 2007). Both the instream and riparian plant communities are also dependant on the finer grained sediments, such as clays, silts and sands, again due to the rich soils they form (Rosenau and Angelo, 2007). As well as this, the fish communities are directly affected by changes to the sediments. The extremely large populations of pink salmon spawning are directly dependent on the gravel bed; the spawning habitat of white sturgeon is dependent on the clean substrate found in secondary channels, and the suspension of fine sediments within the turbulent flows of the spring freshet protect their incubating embryos (Rosenau and Angelo, 2007).

The sediments within the Fraser also play an important role for the construction industry. Within British Columbia the aggregation and extraction of sand and gravel pit operations is valued at ~$170 million, and employs around 4000 people (Rosenau and Angelo, 2007). Commercial gravel mining has taken place in the Fraser since the 1950s, with the majority of sediments being removed from dry gravel bars; the aggregate extraction increased to over 100,000 $m^3$ in the later part of the $20^{th}$ century, being used for local construction and the building of channel defences (Rosenau and Angelo, 2007). The damage caused through extraction of sediments from within the channel as well the riparian areas and islands has a clear and direct impact on the vegetation and biological communities; however there may also be impacts on the fluvial processes related to the natural wandering and erosion of the gravel reach of the Fraser (Rosenau and Angelo, 2007).

## 4.2 Field Data Collection

A field campaign was carried out in March 2012 to obtain contemporary ground truth data. The fieldwork provided geolocated grain size information, which was later used for calibration and validation of grain size data derived from the aerial imagery (Carbonneau *et al*., 2004). Firstly, a set of surface samples were collected for sieve analysis, and secondly a set of ground level photographs (GLPs) were acquired for later analysis.

### 4.2.1 Grain-size Sampling Sites

In the field, 23 sites were randomly selected for surface grain size analysis; these sites were on Queens Bar, N-Bar, Harrison Bar and Calamity Bar. At each of these sites a rectangular frame was applied over a $1 \times 0.8$ m area. This area was subsequently painted, and the surface grains were collected and sieved using the paint-and-pick technique (Lane and Carlson, 1953; Church *et al*., 1987). Field templates were used for sediment larger than 8 mm, with the remaining fraction sieved in the laboratory (samples were sieved to 1.41 mm); weights were calibrated to particle counts and converted to a full distribution (see Appendix 1). 14 sand sites (< 2 mm) were also identified and geolocated, yielding a total of 37 sites.

### 4.2.2 Ground Level Photography

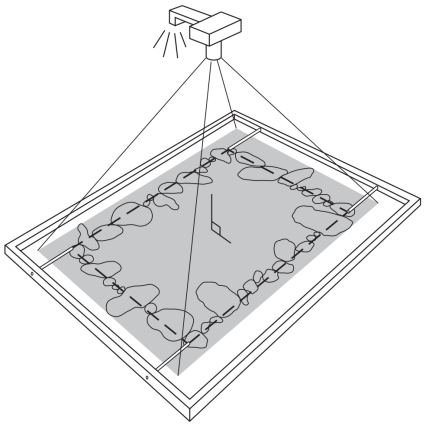

**Figure 6:** *Illustration of the method used to collect Ground Level Photography data (from Graham* et al*., 2005b).*

Due to the substantial time and effort required for collecting and sieving full surface samples, a secondary dataset of ground level photographs was collected to provide further ground truth data. This data set consisted of 223 ground level photographs, collected using the method illustrated in Figure 6 from Queens bar, N-Bar, Harrison Bar and Calamity bar. For both datasets described above, each site location was established with a Trimble 5700 Real Time Kinematic differential Global Positioning System (GPS). Post-processing of the GPS data was carried out using the Canadian Spatial Referencing System (CSRS) online GPS Processing service (`http://www.geod.nrcan.gc.ca/products-produits/ppp_e.php`). With an integrated base station time of around 7 hours in the field, the GPS points have an estimated accuracy of around ±2 cm. The shorter integration time of the Global Positioning System base station on one of the field days meant that the locational precision of a portion of this dataset (GLPs from Queens bar) was lower than expected (around ±1 m).

The final dataset consisted of 153 GLPs covering a range of grain sizes, with a locational accuracy of ±2 cm. The absence of data from Queens bar did not significantly influ-

ence the dataset, as the full range of grain sizes was still covered in the remaining GLPs. Following the aerial image acquisition (see section 4.3), several GLPs were located outside of the coverage of the aerial imagery; the GLP dataset was further trimmed, with 98 GLPs remaining within the coverage area. The GLP data was analysed with both the Sedimetrics package (Graham *et al.*, 2005a,b) and manual photosieving. The manual photoseiving consisted of distributing 100 points randomly across the image, and measuring the grain under each point implemented through a GUI within a MATLAB environment (MathWorks, 2012). GLPs were also collected prior to carrying out the paint-and-pick technique at each of the field sieved sites. Therefore, to provide an accuracy assessment, both photosieving techniques (Sedimetrics and random sampling) were carried out on the images collected at the field sieved sites allowing comparison of laboratory and photosieving derived distributions.

## 4.3 Aerial Image Acquisition

For this study hyperspatial imagery was acquired over several gravel bars within the gravel reach of the Fraser River. This imagery was acquired by DTM Mapping Corporation (`http://www.dtm-global.com`) in March 2012. The imagery was collected using a Vexel Imaging UltraCamX, at a spatial resolutions of 3cm and 10cm (10cm imagery was not used in this study). Bands were imaged between approximately 400nm and 900nm (see Figure 7 showing the spectral sensitivity), resulting in a multispectral image, containing bands in Red, Green, Blue and Near-Infared (NIR).

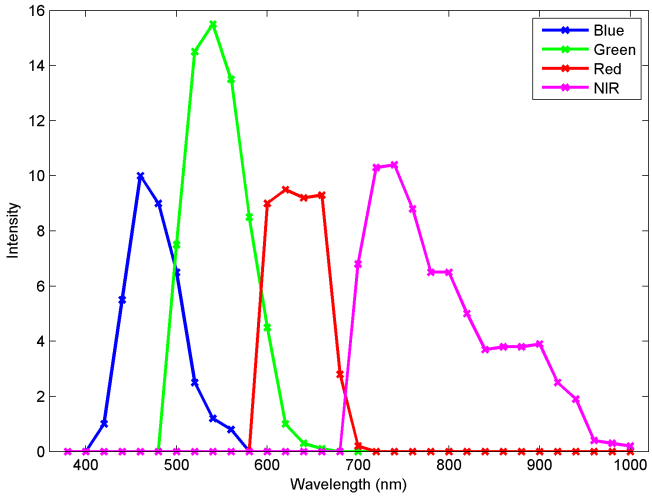


**Figure 7:** *Spectral sensitivity of bands imaged by the UltraCamX (DTM Mapping Corp., 2012).*

Orthorectified image tiles were supplied, and these image tiles are the primary dataset in this study. Following the collection of raw imagery, image enhancement was performed during the orthorectification stage. An image dodger was applied to the 60% overlap region of the imagery; this technique balances the differences in the histograms of the overlapping region of the images, with corrections resulting in a continuous tone image and seamless edges to the resulting mosaic. Images were automatically mosaicked and rectified, producing image tiles covering the entire area (DTM Mapping Corporation, *personal comm.*). Figure 8 shows the coverage of the imagery and the locations of the main gravel bars.

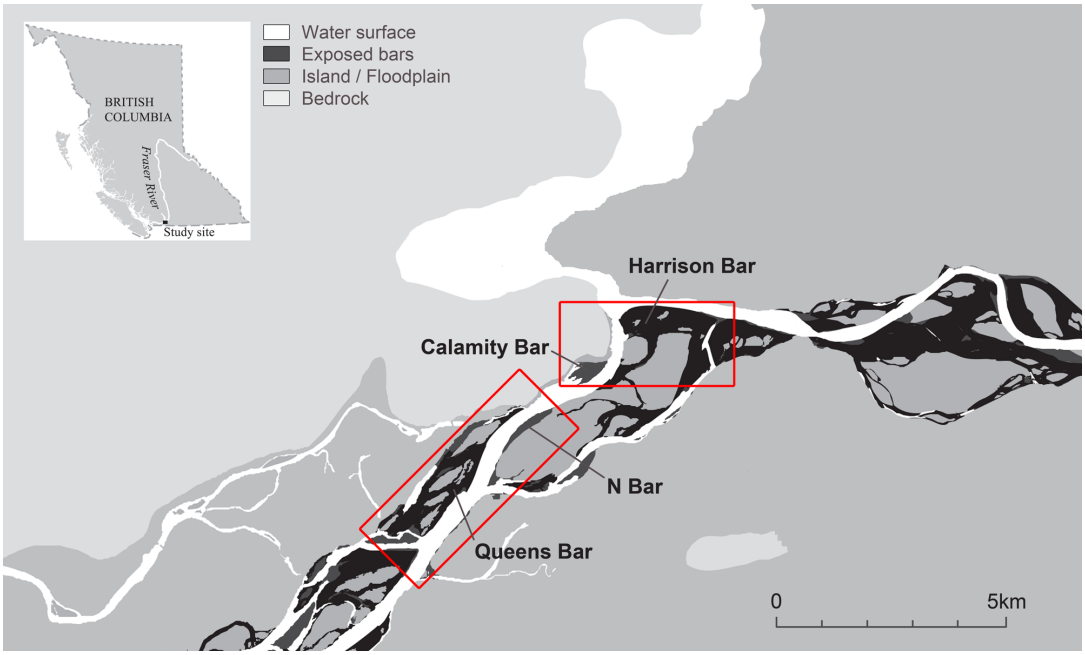


**Figure 8:** *Image showing coverage of the imagery (red boxes) and the main gravel bars. Adapated from Rice and Church (2010).*

### 4.3.1 Grain Size Calibration: Sand

The relationship between image texture and sand was investigated using a 3 × 3 local standard deviation filter (e.g Chandler *et al.*, 2004). Multiple texture values from this standard deviation filter were calculated for known sand points, as well as gravel points. Calibration between texture values and sand was investigated to assess the link between low texture values and the presence of sand. As there were a relatively limited number of sand points, accuracy assessment took place by comparing sand areas produced through calibrated texture equations, to manually delineated sand maps. These sand maps were binary images, wherein a pixel value of 1 is sand and a value of 0 is not sand. Assessment was calculated using a figure of merit (e.g. Pontius *et al.*, 2008) to give a percentage accuracy of classification of 'sand' pixels, as shown in Equation 11

$$FoM = \frac{px_{ov}}{px_{un}} \tag{11}$$

where $px_{ov}$ is the number of overlapping pixels in the manually delineated image and the texture calibrated image, and $px_{un}$ is the number of unique pixels in either image (i.e. pixels representing both errors of commission and omission). Rather than simply provide a percentage of correctly identified pixels, the figure of merit ($FoM$) method takes into account errors of both commission and omission, by including pixels which have either been erroneously classified (commission) or not classified (omission).

### 4.3.2 Grain Size Calibration: Gravel

Calibration with gravel percentiles was assessed using a first order standard deviation filter at a range of window sizes, and second order texture measures through the GLCM. There are several parameters to consider when calculating a GLCM; window size $f(x, y)$, directional offset $O(x, y)$, grey levels $L$, as well as the channel of the image used (R, G, B, NIR) and the statistic calculated. In order to reduce the number of GLCM calculations to a feasible level of processing time, a defined parameter space was investigated. Following the recommendations of Clausi (2002), the 'preferred statistic set' will be investigated; GLCM contrast, correlation and entropy (Equations 3, 4, and 7 in Table 1). As a compromise between computational power and image texture information, Grey Levels, $L$, were fixed at 64. Table 2 shows the remaining parameters investigated. Offsets are given as $O(x, y)$ and calculated when $O(x, y) < \frac{f(x,y)}{2}$. A symmetric GLCM was calculated (Haralick *et al.*, 1973); for example, the sum of two GLCM's with offsets $O(0, +1)$ and $O(0, -1)$ is equal to the symmetric GLCM of $O(0, +1)$.

| **Window Size,** $f(x, y)$ | **Statistics** | **Offset** $x$ | **Offset** $y$ | **Image Band** |
|---|---|---|---|---|
| $3 \times 3$ | Contrast | 0 | 0 | Red |
| $5 \times 5$ | Correlation | 1 | 1 | Green |
| ... | Entropy | ... | ... | Blue |
| $35 \times 35$ | | 8 | 8 | Near Infared |

**Table 2:** *List of parameters used in the Grey Level Co-occurrence Matrix calculations.*

Image texture was calculated on a set of sub-sampled images. These images, *the lab images*, were first extracted from the full aerial image mosaic, around the centre point of the lab grain size samples - thus there were 23 gravel sites with a full laboratory distribution and 14 sand sites (section 4.2.1), each with an associated image. The images were extracted at the same 3 cm resolution as the mosaic, however only a $150 \times 150$ pixel area was extracted (6.75 $m^2$ in real terms), to reduce GLCM computation time. The full parameter space outlined above led to a total of over 450,000 texture calculations.

To investigate the calibrations between texture and the gravel portion of the grain size distribution texture was calculated on all 24 lab images, and linear regression was used to calibrate image texture with the percentiles $D_5$, $D_{16}$, $D_{35}$, $D_{50}$, $D_{65}$, $D_{84}$ and $D_{95}$ from the laboratory data. The best performing parameters were selected based on the highest $r^2$ and lowest Mean Square Error (MSE). Verdú *et al.* (2005) observed increased accuracy of calibrations with the use of multiple texture measures. To investigate this finding, the best parameter set for each GLCM method (contrast, correlation and entropy) and local standard deviation were selected and Multiple Linear Regression used to assess the calibration of a combination of texture parameters with grain size percentiles. As this data set is limited in size, to assess the quality of the final calibrations *leave-one-out cross validation* (Friedman *et al.*, 2001) was used to give a precise estimate of MSE (cross-validated Mean Square Error: $MSE_{cv}$).

# 5 Results

## 5.1 Field Sieving and Ground Level Photography grain-size Information

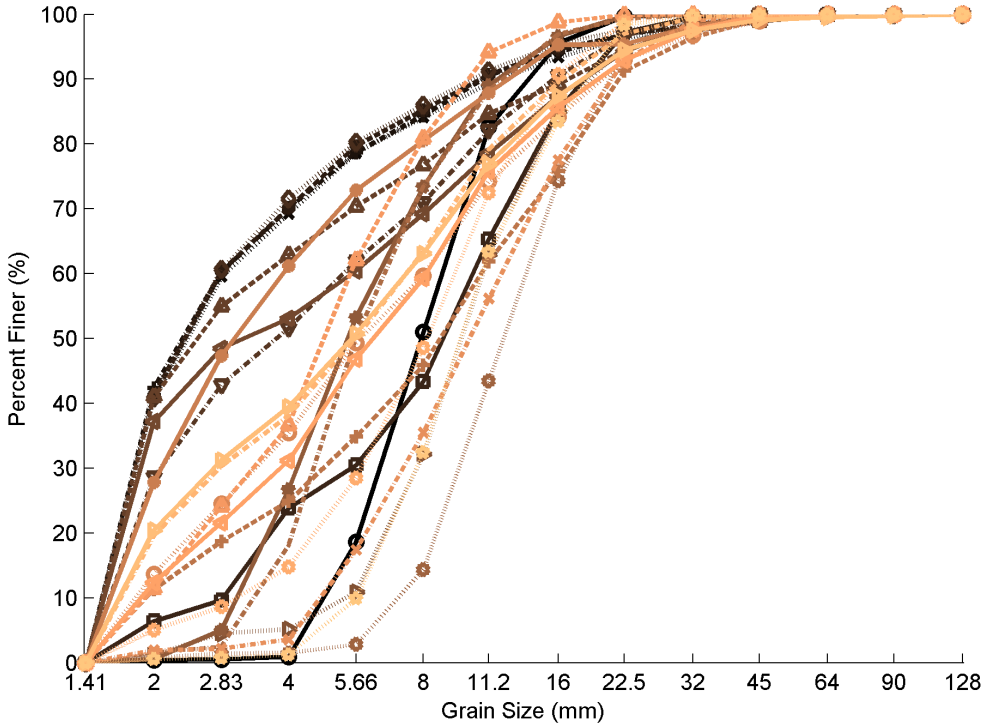


**Figure 9:** *All 23 gravel grain size distributions.*

Figure 9 shows the results of the field sieving for all 23 gravel sites, truncated at 1.41 mm. As can be seen from the plot there is a greater range of grain sizes measured in the lower percentiles, with increasingly narrow range towards the upper percentiles; by $D_{95}$, there is a much smaller range. Table 3 shows some basic statistics, with percentile data being linearly interpolated between sieve data points shown in Figure 9. As well as the 23 sites shown above, 14 sand sites (grain size < 2 mm) were geolocated using a differential GPS (see section 4.2). Grain size data was also derived from the 153 GLPs; data was processed through both the Sedimetrics package and process of manual photoseiving (see section 4.2.2).

| | $D_5$ | $D_{16}$ | $D_{35}$ | $D_{50}$ | $D_{65}$ | $D_{84}$ | $D_{95}$ |
|---|---|---|---|---|---|---|---|
| Min | 1.52 | 1.75 | 2.24 | 2.73 | 3.62 | 6.58 | 15.23 |
| Max | 2.04 | 2.89 | 4.41 | 5.89 | 8.44 | 13.40 | 23.41 |
| Range | 0.52 | 1.14 | 2.17 | 3.16 | 4.82 | 6.82 | 8.18 |
| Mean | 1.64 | 2.12 | 3.08 | 4.15 | 5.83 | 10.35 | 19.26 |

**Table 3:** *Summary statistics of the 23 laboratory grain size samples. Data shown in mm.*

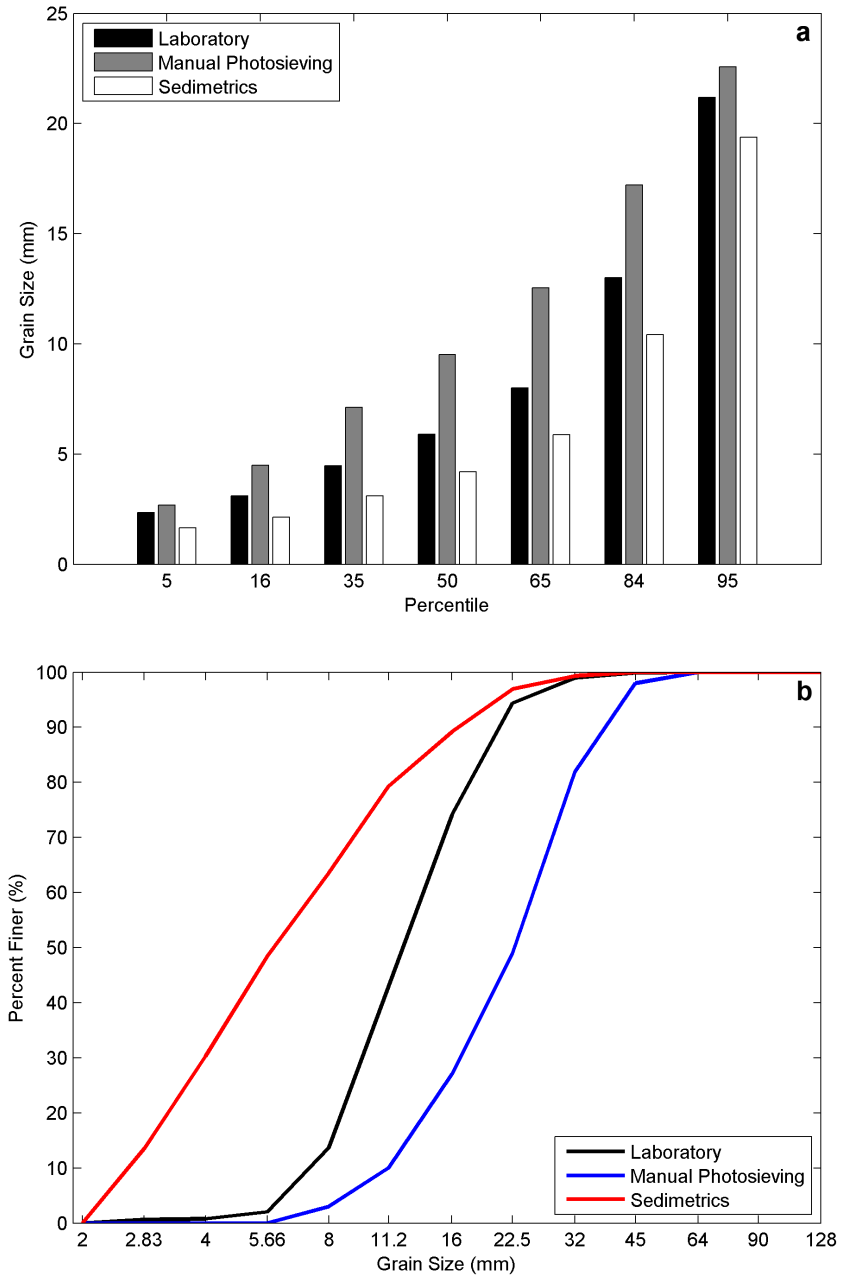


**Figure 10:** *A comparison of distributions derived through photosieving techniques and laboratory measurements. (a) shows average results for each percentile, and (b) shows a site specific example.*

To give an indication of the precision of photosieving techniques, the field sieved sites were also photosieved, through both manual photosieving and the Sedimetrics package (Graham *et al.*, 2005a,b). However, as the aim was to address the sub-pixel portions of the grain size distribution, the Sedimetrics package was used to derive distributions down to 2 mm, which exceed the authors recommendations of a 16 mm truncation (Graham *et al.*, 2005b). Nonetheless, the 23 field sieved sites were processed through both techniques. Figure 10b shows an example of the results for one site. As can be seen, the distributions derived through both the Sedimetrics package and the manual photosieving technique produce vastly different results in comparison to the laboratory results.

## 5.2 Grain Size Calibration: Sand Fraction

The relationship between sand and texture was assessed through a 3 × 3 local standard deviation filter (e.g. Chandler *et al*., 2004). Texture values were also calculated at GLP sites (known to be gravel), to facilitate comparison between texture values for sand / not sand sites. Figure 11 show the results of texture values for sand and not sand sites, calculated on the Red and Near Infared bands.

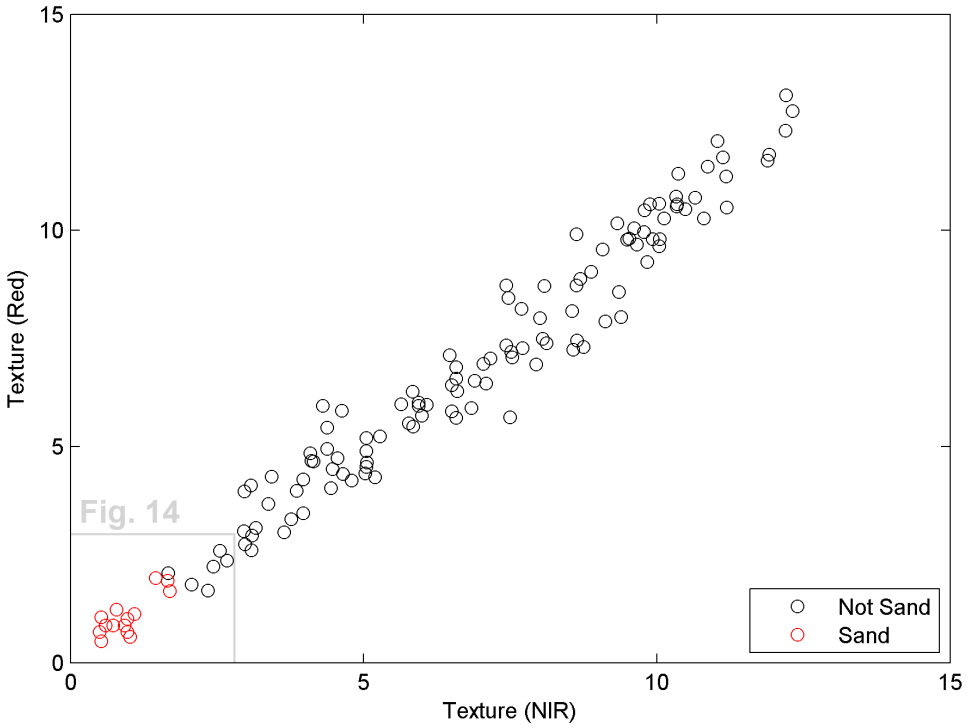


**Figure 11:** *Red and Near Infared texture values for Sand / Non Sand sites.*

## 5.3 Grain Size Calibration: Gravel

### 5.3.1 Local Standard Deviation

A local standard deviation filter was applied at a range of window sizes from $3 \times 3$ in steps of 2 px, to $95 \times 95$ px, on each band. A larger range of window sizes was investigated due to the speed of calculating a standard deviation texture image compared to the GLCM methods. As well as this, the parameter space is much smaller as the range of input parameters is reduced to two (band and window size), unlike the larger range of inputs for a GLCM. The results of calibrations with grain size percentiles are shown in Table 4. Reasonable results are seen up to $D_{50}$, with $r^2$ values decreasing and MSE values increasing for $D_{65}$ and above. As can be seen, lager window sizes produce better calibrations for the lower and mid percentiles, with window sizes reducing for the higher percentiles. With the exception of $D_{84}$, the near infared band produces the best calibrations.

| | $D_5$ | $D_{16}$ | $D_{35}$ | $D_{50}$ | $D_{65}$ | $D_{84}$ | $D_{95}$ |
|---|---|---|---|---|---|---|---|
| $r^2$ | 0.62 | 0.68 | 0.66 | 0.63 | 0.58 | 0.36 | 0.12 |
| **MSE** *mm* | 0.01 | 0.04 | 0.16 | 0.39 | 0.88 | 2.55 | 5.15 |
| **Window Size** $f(x, y)$ | 55 | 55 | 57 | 55 | 25 | 25 | 3 |
| **Band** | NIR | NIR | NIR | NIR | NIR | Green | NIR |

**Table 4:** *Calibration results for each percentile, and associated local standard deviation parameters.*

### 5.3.2 Grey Level Co-occurrence Matrix Linear Regression

Table 5 shows the best results of calibrations following the investigation of the parameter space outlined in section 4.3.2, for each GLCM and percentile. As can be seen, more precise calibrations are achieved for the lower percentiles, with MSE as low as 0.01 mm, and $r^2$ at 0.69 for $D_5$. The calibrations start to deteriorate at the larger percentiles of $D_{84}$ and $D_{95}$, with higher MSE and lower $r^2$ values. Smaller windows sizes achieve better results for the upper and lower percentiles ($D_5$ and $D_{95}$), with a window size of 29 performing the best for the low to mid percentiles. Offsets show a general trend to the North-East / South-West (symmetric GLCMs were calculated in all cases). The Near Infrared band yields the highest calibrations in the majority of cases, with green and blue bands used at the lower and upper percentiles, respectively. The statistic of entropy is also used in the lower and upper percentiles, with contrast best in the mid percentiles, and correlation at $D_{84}$.

| | | **W** | **Ox** | **Oy** | **Band** | $r^2$ | **MSE** (*mm*) | |
|---|---|---|---|---|---|---|---|---|
| **CORRELATION** | $D_5$ | 3 | 2 | 1 | 1 | 0.63 | 0.01 | |
| | $D_{16}$ | 3 | 2 | 1 | 1 | 0.64 | 0.05 | |
| | $D_{35}$ | 3 | 2 | 1 | 1 | 0.59 | 0.20 | |
| | $D_{50}$ | 3 | 2 | 1 | 1 | 0.50 | 0.52 | |
| | $D_{65}$ | 25 | 6 | 2 | 2 | 0.41 | 1.23 | |
| | $D_{84}$ | 23 | 6 | 3 | 2 | 0.56 | 1.74 | * |
| | $D_{95}$ | 5 | 1 | 2 | 1 | 0.40 | 3.52 | |
| **CONTRAST** | $D_5$ | 29 | 2 | 6 | 4 | 0.59 | 0.01 | |
| | $D_{16}$ | 29 | 2 | 6 | 4 | 0.66 | 0.04 | * |
| | $D_{35}$ | 29 | 2 | 7 | 4 | 0.68 | 0.16 | * |
| | $D_{50}$ | 29 | 3 | 7 | 4 | 0.68 | 0.33 | * |
| | $D_{65}$ | 29 | 3 | 7 | 4 | 0.66 | 0.72 | * |
| | $D_{84}$ | 29 | 6 | 0 | 2 | 0.46 | 2.16 | |
| | $D_{95}$ | 15 | 1 | 0 | 2 | 0.27 | 4.27 | |
| **ENTROPY** | $D_5$ | 5 | 1 | 2 | 2 | 0.69 | 0.01 | * |
| | $D_{16}$ | 31 | 3 | 2 | 4 | 0.63 | 0.05 | |
| | $D_{35}$ | 31 | 3 | 2 | 4 | 0.60 | 0.19 | |
| | $D_{50}$ | 29 | 5 | 5 | 4 | 0.55 | 0.47 | |
| | $D_{65}$ | 29 | 5 | 5 | 4 | 0.49 | 1.08 | |
| | $D_{84}$ | 29 | 8 | 4 | 2 | 0.22 | 3.11 | |
| | $D_{95}$ | 15 | 6 | 7 | 3 | 0.43 | 3.35 | * |

**Table 5:** *Calibration results for each percentile, and associated GLCM parameters. Table headings are as follows;* ***W****, Window size* $f(x,y)$*;* ***Ox*** *and* ***Oy****, Offsets (x) and (y) respectively, Band where numbers 1-4 represent Red, Green, Blue and NIR respectively. Rows marked with an asterisk highlight the best calibrations for each percentile.*

### 5.3.3 Multiple Linear Regression

To investigate the use of Multiple Linear Regression for grain size calibration, the best performing parameters were selected for each GLCM method (contrast, correlation and entropy), and combined with the best performing standard deviation measure (see Table 5 for the full parameter list). Multiple Linear regression was then used with these parameters, and the results were subsequently cross-validated. The results are shown in Table 6[1]. The highest $r^2$ and lowest MSE values are found in the lower percentiles, with the best calibration found for $D_5$. Reasonable calibrations are seen up to $D_{65}$, with MSE at 21%. Calibrations are poorest for $D_{95}$, with MSE at 45%. For each percentile, the grain size was calculated and compared to observed grain size; Figure 12 shows the results. The spread of data in these plots explains the $r^2$ and MSE values found for each of the percentiles; a wider scatter of data from the $y = x$ line results in larger MSE and lower $r^2$ values. This effect can be seen in the larger percentiles, particularly $D_{95}$.

| | $D_5$ | $D_{16}$ | $D_{35}$ | $D_{50}$ | $D_{65}$ | $D_{84}$ | $D_{95}$ |
|---|---|---|---|---|---|---|---|
| **r2** | 0.92 | 0.80 | 0.68 | 0.77 | 0.76 | 0.68 | 0.56 |
| **MSEcv** | 0.01 | 0.04 | 0.21 | 0.51 | 1.03 | 1.80 | 3.68 |
| **MSEcv (%)** | 0.61 | 3.55 | 9.85 | 16.25 | 21.39 | 26.43 | 44.99 |
| $K$ | 2.7452 | 2.6698 | 4.1344 | 2.0222 | 1.5056 | 10.0058 | 3.0520 |
| $E$ | -0.2827 | 0.1659 | 0.1924 | 1.2114 | 1.6302 | 0.8785 | 3.9362 |
| $C_R$ | 0.0592 | -0.1857 | 0.0000 | -0.2274 | -6.9821 | -15.7642 | 4.2777 |
| $C_N$ | 0.0045 | -0.0072 | -0.0336 | -0.0965 | -0.1921 | -0.0833 | -0.2521 |
| $S$ | -0.0355 | -0.0897 | -0.1077 | -0.1307 | 0.0682 | -0.0838 | 0.0481 |

**Table 6:** *Multiple Linear Regression Calibration and Cross Validation results for each percentile. K represent a constant added to each value, and the remaining rows represent the multiplicative coefficients for the texture methods; Entropy, E, Correlation, $C_R$, Contrast, $C_N$ and Standard Deviation, S.*

[1] $\text{MSE}_{CV}$ (%) is calculated as $\text{MSE}_{CV}$ / ($\text{MAX}_{mm} - \text{MIN}_{mm}$), for each percentile.

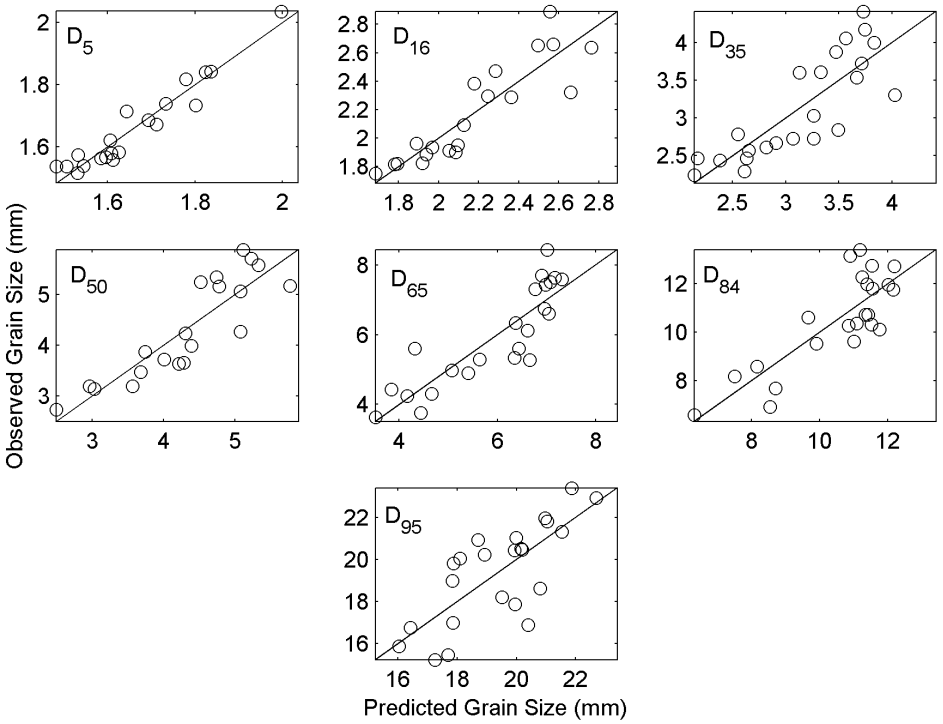


**Figure 12:** *Predicted vs Observed Grain Size for each percentile.*

## 5.4 Grain Size Maps

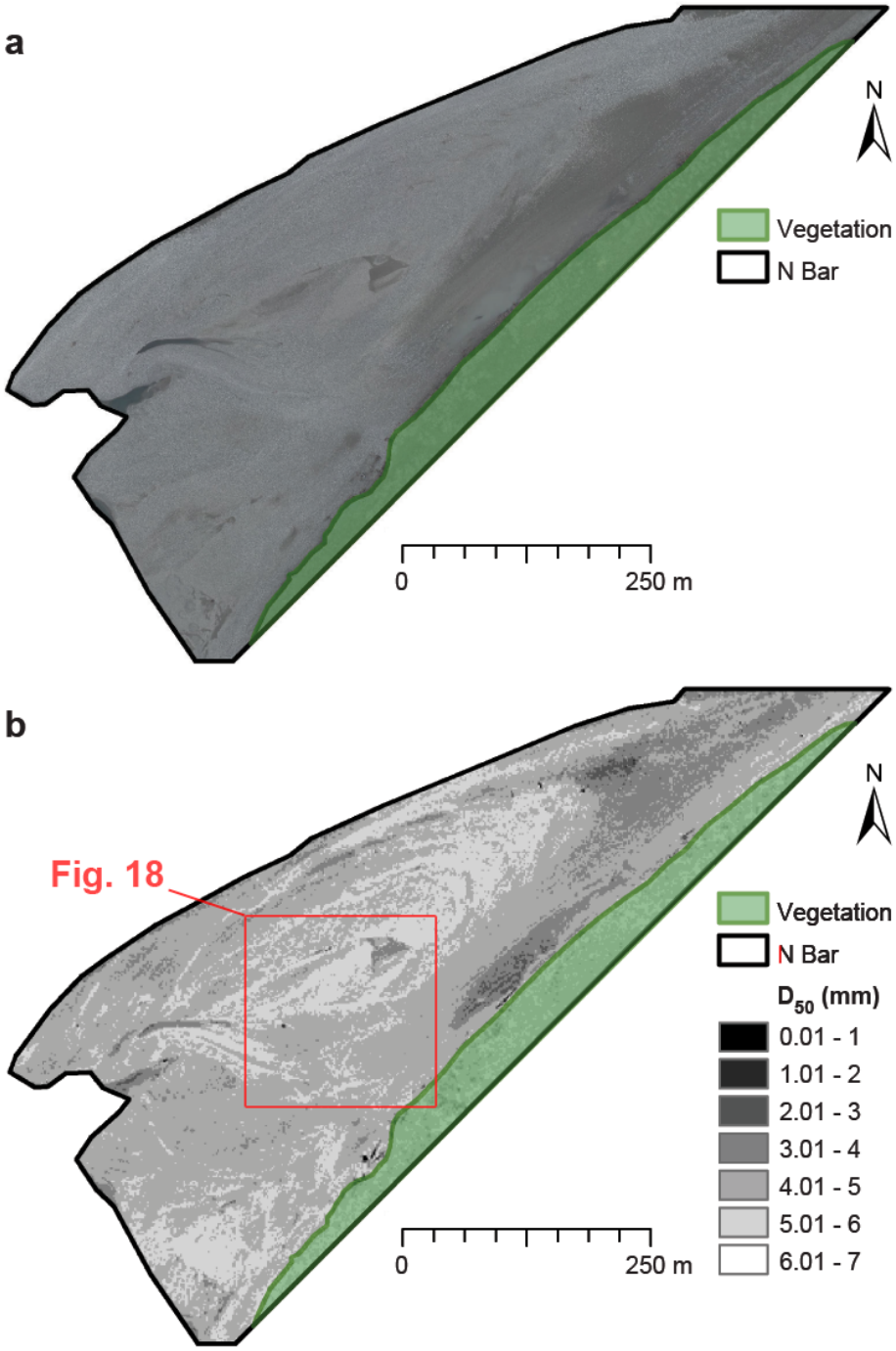


**Figure 13:** *N Bar: Hyperspatial imagery of the bar (a) and $D_{50}$ grain size map (b).*

Figure 13 shows a sample $D_{50}$ map produced using multiple linear regression of four texture layers, with optimal parameters as derived from the investigation of GLCM parameters described in Section 5.3. Similar maps were also calculated for the remaining percentiles; $D_5$, $D_{16}$, $D_{35}$, $D_{65}$, $D_{84}$ and $D_{95}$. These percentile maps combined with a binary classification layer of sand resulting in a 'multispectral' grain size image, reproducible for the entire reach, at a spatial resolution of 1.65 m. Thus a 7 point grain size distribution can be extracted, along with large scale estimates of surface sand content (through the binary sand classification).

# 6 Discussion

## 6.1 Field Sieving and Ground Level Photography data

Following an investigation into photosieving techniques, it was found that results were poor, with distributions not reflecting the laboratory data (Figure 10a and b). Overall, the techniques of Graham *et al*. (2005a,b) performed marginally better than manual photosieving, however performance was consistently poor for the finer grained material. On average, manual photosieving techniques produced constant over estimation, whilst Sedimetrics produced an underestimation (Figure 10a). As noted by Graham *et al*. (2005a) one grain must occupy at least 23 pixels to be measured reliably - the GLP dataset had an approximate pixel resolution of 0.35 $mm^2$, suggesting that reliable measures will only occur for grains 8 mm and above. The manual photosieving technique involved sampling 100 random grains, *with replacement*. The effect of sampling with replacement may have acted to increase the influence of the larger grains on the final distribution, given their greater occupancy in an image, and therefore greater chance of repeat measurement. Improvements were seen for both techniques with various truncations up to 16 mm, however, given the focus on the finer grains and particularly the sand fraction, it was decided not to analyse the GLP dataset any further.

## 6.2 Grain Size Calibration: Sand

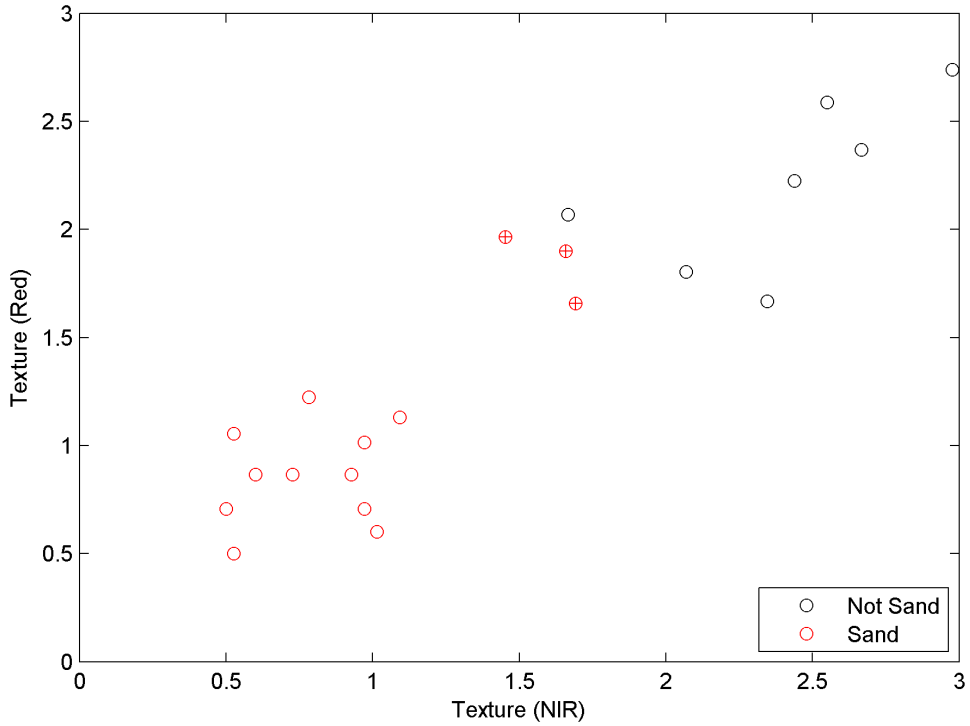


**Figure 14:** *Detailed graph of sand - non sand data points, with anomalies highlighted (crossed circles). See Figure 11 for full data range.*

Investigation of image texture and sand (< 2 mm) revealed a simple, inequality-based relationship following the removal of anomalies. Figure 14 shows an expanded portion of Figure 11, highlighting the anomalous values. The anomalous points were investigated due to their texture values being significantly higher than the remaining points, which were clustered between 1 and 1.4. Investigation of the imagery, shown in Figure 15, reveals the cause of the higher texture values. Within the gravel reach of the Fraser, the majority of gravel bars are accessible by vehicles; they are widely used for recreational activities, which are particularly focused on homogeneous areas of sand and other finer grained material, due to the ease of access for large 4×4 vehicles, motorbikes and All Terrain Vehicles (ATVs). Each of the anomalous points in question have higher texture values due the impact of tyre tracks, and wet/dry sand transitions, as can be observed in Figure 15.

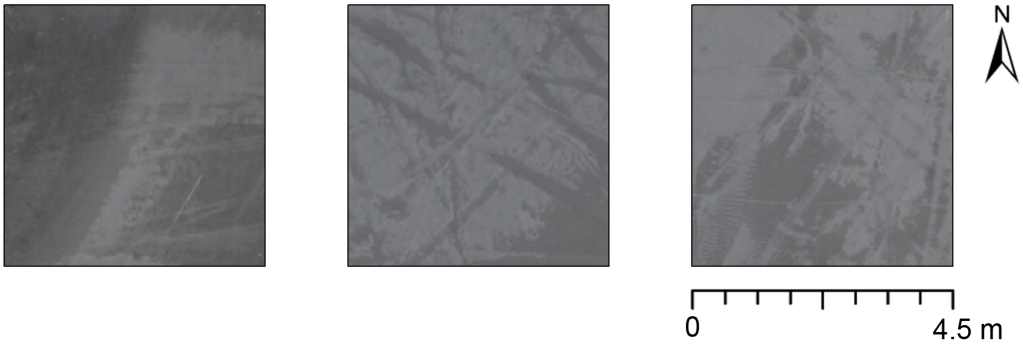


**Figure 15:** *Raw imagery for the anomalous points.*

Removing anomalies, texture values calculated for sand points did not exceed 1.48 across all bands (Figure 11 shows this for the red and NIR bands). Thus, sand can be calculated through application of Equation 12

$$map(x,y) = \begin{cases} 0 & \text{if } tx(x,y) > 1.48 \\ 1 & \text{if } tx(x,y) \leq 1.48 \end{cases} \tag{12}$$

where $tx$ is the texture value at the point $(x, y)$ on a $3 \times 3$ standard deviation filtered image, and a value of 1 at point $(x, y)$ on the produced $map$ denotes the presence of sand. The application of a $3 \times 3$ filter means surface sand maps can be produced with an approximate spatial resolution of 27 cm$^2$. Given the significant effect of human influence upon texture values, equation 12 may only be applicable to areas of undisturbed sand. Nonetheless, a section of Calamity Bar was selected as a test site to produce a surface sand map; as it is only accessible by boat there is limited human disturbance of the sand surfaces. The Calamity test area was selected due to a large homogeneous zone of sand which is easily distinguishable. Figure 16 shows the raw imagery (a) and resulting surface sand map (b) generated through a binary classification using equation 12. Assessment through the $FoM$ showed a 70.05% classification accuracy.

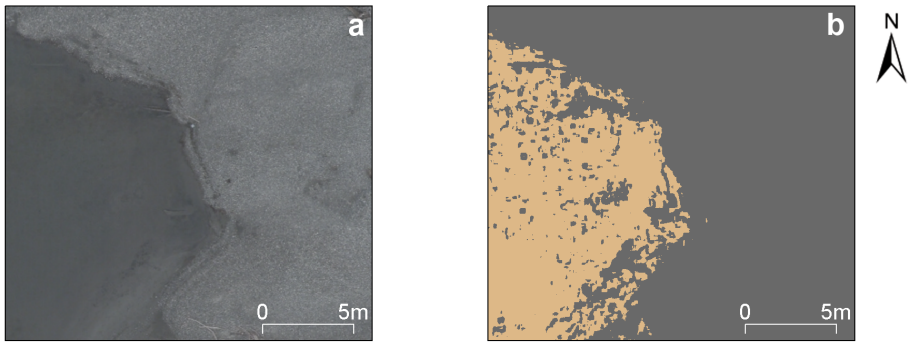


**Figure 16:** *Calamity Bar: Raw Image (a) and subsequent sand classification (b), where sand areas are shown in beige.*

Investigations into several of test areas from the full range of gravel bars yielded a final $FoM$ classification accuracy of 70% ± 10%. These findings suggest that even a simple inequality based calibration of texture can yield relatively accurate maps of surface sand content. Equation 12 could be improved with a larger number of input sites, and more detailed investigation into sites which may have artificially high texture values due to human disturbance. However, these results support the findings and suggestions of Chandler *et al*. (2004), such that there is enough information present in standard colour imagery to yield accurate maps of surface sand content. Accuracies achieved here represent an improvement on those presented by Chandler *et al*. (2004) in terms of sand classification; likely due to the improved image quality (aerial imagery used here was acquired in dry conditions with consistent lighting) and simple binary classification approach. This approach is beneficial for several reasons. Computations are not particularly complex, meaning large images can be easily and quickly processed, enabling rapid mapping of entire reaches. The sand calibrations derived here are strongly applicable to grey-scale imagery as only one input is required for the computation of texture, with strong results found, independent of the band used; this allows for potential exploitation of the large archive of grey-scale imagery, useful for change detection. However, it must also be noted that the hyperspatial resolution of the imagery used is a key factor – imagery with a coarser spatial resolution may not perform as well, thus a repeat accuracy assessment would be required.

The ability to produce surface maps of sand is important due to the uncertainties in the current sediment budget in the Fraser (Ham, 2005), and the importance of percentage sand as a key parameter in defining hydraulic and transport characteristics in gravel-bed rivers (Chandler *et al*., 2004). The method generated here improves on currently available techniques for surface sand mapping, and provides an interesting insight into the ability to extract sub-pixel grain size information from hyperspatial imagery. There are several caveats to consider, however. Tyre tracks and other features such as wet/dry sand transitions and transitions between grain size classes exert a significant influence on image texture, resulting in a known source of classification error; one which remains very difficult to discriminate and account for without manual classification. Similarly, natural features such aeolian bedforms or ripples within sand may result in larger image texture

values which could also lead to misclassification. The use of a 3 × 3 texture window implies that sand areas must be somewhat homogeneous if they are to provide a distinct textural signature, therefore the ability to discriminate interstitial/mixed sand and gravel patches remains an area for investigation. Simple image texture and classification approaches are currently not capable of this, however, ever increasing image resolution may eventually resolve this issue; as long as enough pixels make up a homogeneous area of grains, a textural signature will be present.

It is important to note that the threshold value established here (Equation 12) can be modified depending on the users desired accuracy. As noted above, areas where abrupt changes occur (such as wet/dry sand, tyre tracks and so on) will act to change pixel intensity values occur and therefore may be misclassified; this could be the case even within areas entirely composed of sand; shadows cast on the stoss or lee side of dunes and ripples, transitions from wet-to-dry sand, and man-made human features such as tyre tracks are just a few possible examples which could be misclassified. Therefore, it is recommended that threshold values be adjusted depending on the imagery and the users desired accuracy of surface sand mapping. For example, in order to classify all areas of surface sand the user may select a slightly higher threshold value with the knowledge that there be some errors of commission (such as homogenous areas of fine gravel which may produce a low textural signature, may hence be classified as sand; e.g. Figure 14).

## 6.3 Grain Size Calibration: Gravel

Grain size calibrations for the gravel fraction provide an interesting link to image texture. A combined Multiple Linear Regression approach encompassing all texture measures provides the best calibrations, a similar finding to Verdú *et al*. (2005). Comparing Table 5 and 6 reveals that much stronger calibration result following MLR. Whilst absolute MSE values appear higher post-MLR, this is simply an artefact of the use of cross validated Mean Square Error at the MLR stage. Actual calibrations are improved, and this is observed by inspecting Figure 12. As noted (Section 5.1), all of the derived grain size percentiles are very much below the image resolution of 30 mm. Interestingly, calibrations become much weaker as the pixel resolution is approached (e.g. $D_{95}$), with the strongest calibrations found for the lower percentiles; the best results are seen for $D_5$, and some theoretical considerations are given below. Table 7 shows the input parameters for $D_5$.

Smaller window sizes are required for the methods of entropy and contrast, with larger window sizes for correlation and standard deviation, whilst offsets remain in a North-East / South-West orientation (using a symmetric GLCM). The method of entropy is related to the probability of pairs of pixel values in the GLCM; a random distribution of pixel pair probabilities would yield maximum entropy. In the context of $D_5$, entropy in a small window assesses how 'scattered' the probability pairs are; entropy values are low for $D_5$, meaning pixel pairs are similar, hence image texture is lower - theoretically, $D_5$ should have 'lower' texture, as it relates to the smaller grain sizes of the distribution; $D_5$ values

in all cases are less than 2 mm (i.e. sand), which should have a smooth texture. Contrast is a weighting of a the intensity difference between a pixel and its neighbour - lower weightings represent similar pixels. A similarly small window size proves the best for contrast, again similar pixels producing lower texture values. For the methods of correlation and standard deviation, larger windows prove the best - correlation measuring the linear dependency of grey levels between pixels and standard deviation measuring the variance from the mean pixel values within that window, without any spatial referencing between pixels (i.e. first order texture). Correlation values are higher for $D_5$ and begin to decrease with larger percentiles, hence identifying the 'smoother' texture that $D_5$ should theoretically have. Across the whole range of percentiles, offsets remain North-East / South-West, probably due to a slight imbrication of grains in the field. Correlation retains the highest offsets of all the methods, in all cases. Appendix 2 contains the parameters for the remaining percentiles.

| Method | Window Size | Offset $x$ | Offset $y$ |
|---|---|---|---|
| Entropy | 5 | 1 | 2 |
| Contrast | 3 | 2 | 1 |
| Correlation | 29 | 2 | 6 |
| Standard Deviation | 55 | N/A | N/A |

**Table 7:** *Input parameters for $D_5$ grain size calibrations.*

All the grain size percentiles are subpixel, therefore several grains will be 'averaged' into one pixel - in homogeneous areas of grains the averaging of larger populations grains into one or more pixels will mostly likely result in several neighbouring pixels sharing very similar characteristics. Hence, larger offsets and window sizes are required to discern patterns of texture. Even the largest of grains will be entirely contained within one pixel; therefore larger scale textural patterns are easier to identify. This could explain the stronger calibrations with the smaller percentiles. The averaging of larger populations of small grains into one pixel, especially in homogeneous patches of sediment, leads to stable pixel values due to the consistency of the sediment over the area of one pixel ($3cm^2$). This stability will also remain when calculating texture and leads to 'smooth' patterns, which theoretically calibrate with lower percentiles as they should have a smoother textural signature. As grain size increases, smaller populations of grains will be contained within one pixel, hence averaging values may show greater variance across several pixels, and less stability in texture values as a result; calibrations may begin to break down.

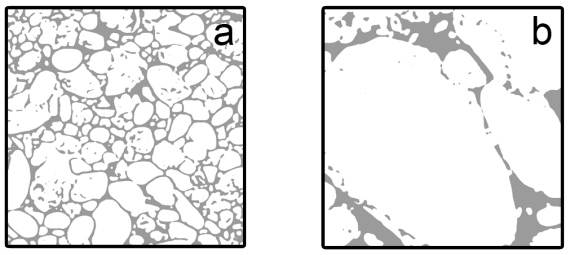


**Figure 17:** *Illustration of the 'pixel averaging effect'; a) shows a large population of smaller grains to be averaged into one pixel (black border represents one pixel), compared to the fewer but larger grains averaged within b).*

However this behaviour may exhibit a threshold effect. Verdú *et al*. (2005) found stronger calibrations for intermediate and larger percentiles ($D_{50}$ and $D_{84}$), however an important point to note is pixel resolution, at 3 mm (on 1:40 scale imagery). This means a single grain makes up several pixels, therefore no averaging effect is present - texture values will directly relate to the size of actual grains, hence calibrations are made directly to grains not to averaged populations of grains within one pixel. Therefore, texture can be split into two groups - 'averaged' pixel texture, and actual grain texture, with the latter being present on higher resolution imagery wherein entire grains make up several pixels. The transition between these two measures will have a direct impact upon calibrations between texture and grain size. The 'averaged' pixel texture pattern will begin to break down as grain size increases towards the pixel resolution - lower populations of grains will be present within one pixel, hence across several pixels of similar grain size, pixel values may show higher variance and calibrations may be unstable. For smaller grain sizes, the higher population of grains within one pixel provides consistency to the averaging effect. As grain size increases, grains will cross a threshold and begin to encompass several pixels - texture values will then be directly related actual size of the grain, and not the 'averaging' of several grains into one pixel. This effect is illustrated in Figure 17, comparing smaller grains averaged into one pixel, compared to larger grains which are approaching the pixel resolution (Figure 17 a and b respectively).

## 6.4 Grain Size Mapping

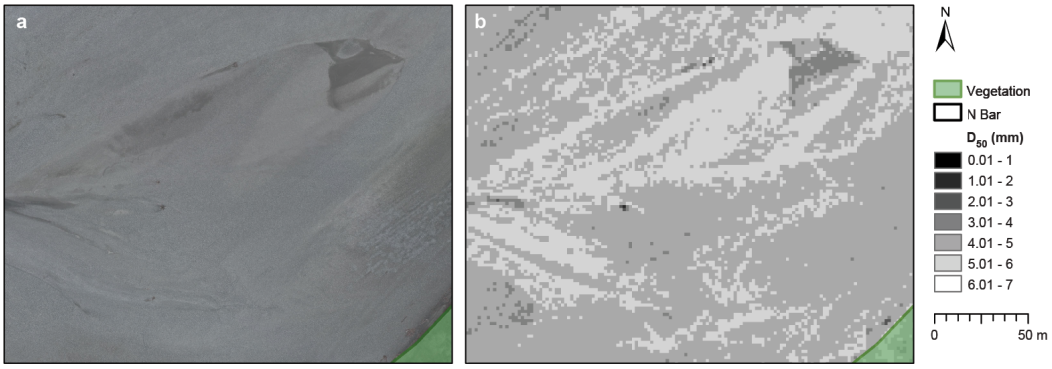


**Figure 18:** *N Bar: An enlarged portion of the grain size map showing imagery (a) and the $D_{50}$ grain size map (b).*

Figure 18 shows an enlarged section of the grain size map calculated for an area of N bar (figure 13), at a spatial resolution of 1.65 $m^2$. Coarser resolution is noted, compared to Carbonneau *et al*. (2004) and Verdú *et al*. (2005), as a result of block processing at larger window sizes. This $D_{50}$ map effectively forms the $5^{th}$ 'band' of a multispectral image, wherein 8 bands are present denoting each of the grain size calibrations, with layer one being a binary classification of sand. This 'multispectral grain size image' can be envisaged similar to a multiband Landsat image. The generated multispectral image can therefore be used to extract either specific percentiles at an $(x, y)$ point, or even to extract all 7 percentiles to form a grain size distribution. Large scale patterns can be identified by looking at individual layers, as can be seen in Figure 18 above; as well as this, large scale maps of surface sand for the reach can be generated. Some limitations are noted, particularly the influence of transitions from homogeneous patches of sand to gravel areas. The transitional zone causes a local increase in texture values which in turn cause an increase in grain sizes which may not actually be present. Similarly, edges of bars where there is a transition to the channel or to vegetation may see this effect. This effect is slightly damped due to the use of block processing at window sizes much larger than the spatial resolution of the imagery.

Following the calculation of texture and calibration to grain size for the remaining images, grain size maps were calculated for the remaining bars within the gravel reach (see Figure 8 and Appendix 3), providing large scale spatial coverage of detailed grain size information at a greater resolution than can be achieved by standard field techniques. Consideration must be given to the MSE values achieved for each percentile, and subsequent errors must be accounted for when using calculated grain sizes for other applications such as modelling. Significant uncertainty exists for the larger percentiles, particularly $D_{84}$ and $D_{95}$, however the finer grained fractions provide fairly precise estimates compared to field sieved data. Specifically within the Fraser these results will provide an improved method of mapping the finer grain fractions over a much greater spatial area, and at a finer resolution than previously possibly. It is anticipated that these results will provide

an improvement to calculated sediment budgets, given the known problems of assessing finer grained material within the sediment distribution.

The applicability of these results to other field sites is difficult to assess, due to the lack of availability of a similar dataset in another location. The same methodology however, may be strongly applicable but calibration and validation would be required. However, some recommendations are as follows. Other study localities and differing scales of imagery, a reduced parameter space is recommended, and consideration must be given to the pixel averaging effect. Multispectral imagery is not necessarily required, as similar relations are found using only standard colour imagery. It is recommended that future studies need only consider the parameters of window size (where the minimum window size is set according to the image resolution), and offsets. Offsets should be investigated with prior knowledge of sediment imbrication in the field, as it is highly likely the optimal GLCM orientation will be coincident with any imbrication. Remaining parameters can be set as desired, following those outlined in this study.

## 6.5 Limitations and Recommendations

Several limitations and sources of potentially unknown error exist within this study, and must be considered. Limited field time prevented the collection of a larger number of field samples – an increased number of sites would provide a better indication of calibrations and other methods of measuring grain size (e.g. Wolman sampling) could have been collected to aid in validation of results, particularly for the sand sites. Within the collection of the field sieved data, there are potential errors. Using the paint-and-pick technique, paint may have penetrated the interstitial space between surface and buried grains, hence some sub-surface grains may have been incorrectly collected and sampled introducing some uncertainty in the results. As well as this, the paint may have adhered smaller, particularly sand and silt grains to larger particles thereby introducing a bias into the finer grained fraction of the distribution (or in some cases it may have acted to remove finer grained material from the sample). Within the laboratory, there are potential sources of error when sieving the finer grained fractions. For example some particles may become permanently stuck within the square sieve holes and thus may have not been included in the final distribution. Conversion of the finer grained material from weights to grain counts may have also introduced slight error within the data.

A particular area of uncertainty exists in reference to the aerial imagery itself. The georeferenced image tiles supplied by DTM Mapping Corporation had undergone some element of pre-processing. Whilst the techniques used were described (DTM Mapping Corporation, *personal comm.*; section 4.3), the actual algorithms and processing techniques remain slightly unclear. Raw, unprocessed image tiles were supplied, however the influence of significant georeferencing issues and lack of perspective correction meant that the raw imagery introduced a much greater source of positional error; given the very strong spatial dependence of both the grain size data and calculated texture values, raw imagery was not

used due to this uncertainty in georeferencing.

Within the computational calculation of grain size calibrations, grey levels were fixed at 64. Whilst this prevents the parameter space from increasing to unfeasible computational time, it still remains an area for investigation. The resampling of grey levels to smaller values such as 16 or 32 may introduce some more stability into texture calculations and reduce grey level noise; similarly expansion of grey levels, such as 128 may act to increase the amount of information present due to less resampling, and as such calibrations may be improved. Ideally, a range of grey levels, up to 256 (no resampling) would be included in the investigated parameter space. Similarly to grey levels, only the independent texture measures suggested by Clausi (2002) were investigated to save computational time. Again, it would be wise to investigate an increased number of methods (see Table 1), with the knowledge that there may be significant redundancy in some layers due to the high correlation between GLCM methods. Computation constraints at the Multiple Linear Regression stage could also be addressed. In this study, the best performing parameter for each GLCM method were selected for grain size calibration, however it would also be wise to investigate all combinations. It is advised that future studies consider these issues as well as several scales of imagery to investigate the 'pixel averaging effect'.

# 7 Conclusion

An investigation of image texture and grain size calibrations has been presented, with the main aim to map sub-pixel grain size information. Research was split into two objectives; to identify a technique capable of mapping surface sand content, and to investigate the feasibility of producing a grain size distribution for the gravel fraction. The main conclusions were as follows:

1. Investigations in reference to the sand fraction reveals a simple inequality based classification of a first order texture measure (standard deviation) to produce binary maps of surface sand content. Validation using a per-pixel accuracy assessment in reference to manually delineated sand areas showed a classification accuracy of 70% ± 10%.

2. The gravel fraction was addressed by expansion of existing techniques; a wide ranging parameter space using a grey level co-occurrence matrix was investigated. The combination of first order and second order (GLCM) texture measures in conjunction with multiple linear regression provided the best calibrations for smaller percentiles (finer grains) of the grain size distribution (i.e. $D_{65}$ and under).

3. For larger percentiles (coarser grains) of the grain size distribution, calibrations began to break down. This was attributed to the 'pixel averaging effect', whereby smaller percentiles had more stable calibrations due to averaging of a larger population of grains within one pixel. Calibrations begin to break down as the pixel resolution is approached, as smaller populations of grains are averaged into one pixel, and greater variance between pixels is introduced as a result.

The methodology presented was used to produce multispectral grain size images. 8-band images consisting of a binary sand class and 7 grain size percentiles were calculated at a spatial resolution of 1.65m$^2$. 'Multispectral Grain Size Maps' were produced for Queens Bar, N Bar, Calamity Bar and Harrison Bar located within the Gravel Reach of the Fraser River. Limitations of the number of field sites for calibration and validation (14 for sand, and 23 for gravel) are noted as a point for expansion in future studies. Computational limitations also prevented investigation of some GLCM parameters (grey levels and statistical methods) and in multiple linear regression calculations; also noted as a point to be addressed in future studies. Overall, this allows for a rapid method of acquiring a 7 point grain size distribution and map of surface sand content for large areas, at a much higher spatial resolution than can be obtained through standard field techniques.

# 8 References


Achar, S., Sankaran, B., Nuske, S. T., Scherer, S. and Singh, S. (2011). Self-supervised segmentation of river scenes, *International Conference on Robotics and Automation 2011*.

Buscombe, D. (2008). Estimation of grain-size distributions and associated parameters from digital images of sediment, *Sedimentary Geology* **210**(1-2): 1 – 10.

Buscombe, D. and Rubin, D. (2012a). Advances in the simulation and automated measurement of well-sorted granular material. part 1: Simulation., *Journal of Geophysical Research* **117**: F02001.

Buscombe, D. and Rubin, D. (2012b). Advances in the simulation and automated measurement of well-sorted granular material. part 2: Direct measures of particle properties., *Journal of Geophysical Research* .

Buscombe, D., Rubin, D. M. and Warrick, J. A. (2010). A universal approximation of grain size from images of noncohesive sediment, *Journal of Geophysical Research* **115**: F02015.

Butler, J., Lane, S. and Chandler, J. (2001). Automated extraction of grain-size data from gravel surfaces using digital image processing, *Journal of Hydraulic Research* **39**(5): 519–529.

Carbonneau, P. E., Bergeron, N. E. and Lane, S. N. (2005). Automated grain size measurements from airborne remote sensing for long profile measurements of fluvial grain sizes., *Water Resources Research.* **41**: W11426.

Carbonneau, P. E., Lane, S. N. and Bergeron, N. E. (2004). Catchment-scale mapping of surface grain size in gravel bed rivers using airborne digital imagery., *Water Resources Research.* **40**: W07202.

Carbonneau, P. and Piégay, H. (2012). *Fluvial Remote Sensing for Science and Management*, Wiley.

Census (2001). The 2001 Census of Canada. Accessed 7$^{th}$ December 2011.
**URL:** *www.bcstats.gov.bc.ca*

Chandler, J. H., Rice, S. and Church, M. (2004). Colour aerial photography for riverbed classification, *The International Archives of the Photogrammetry, Remote Sensing and Spatial Information Sciences*, Vol. 34.

Chang, F. and Chung, C. (2012). Estimation of riverbed grain-size distribution using image-processing techniques, *Journal of Hydrology* **440–441**: 102 – 112.

Church, M. (1983). Pattern of instability in a wandering, gravel-bed channel, *in* J. Collinson and J. Lewin (eds), *Modern and ancient fluvial systems*, International Association of Sedimentology, Special Publication 6, pp. 169–180.

Church, M., Ham, D. and Weatherly, H. (2001). *Gravel Management in lower Fraser River*, Department of Geography, University of British Columbia.

Church, M., McLean, D. and Wolcott, J. (1987). River bed gravels: sampling and analysis, *in* C. Thorne, J. Bathurst and R. Hey (eds), *Sediment transport in gravel-bed rivers*, A Wiley-Interscience publication, J. Wiley.

Clausi, D. A. (2002). An analysis of co-occurrence texture statistics as a function of grey level quantization, *Canadian Journal of Remote Sensing* **28**(1): 45–62.

Deserno, T. (2011). *Biomedical Image Processing*, Biological and Medical Physics, Biomedical Engineering, Springer.

Dugdale, S. J., Carbonneau, P. E. and Campbell, D. (2010). Aerial photosieving of exposed gravel bars for the rapid calibration of airborne grain size maps, *Earth Surface Processes and Landforms* **35**(6): 627–639.

Ellis, E., Church, M. and Rosenau, M. L. (2004). *Characterization of 4 floodplain side channels of the lower Fraser River*, Department of Geography, University of British Columbia, Vancouver, Canada.

Environment Canada (2011). *Fraser River at Mission (08MH024): Hydrometric Data*. Accessed 2$^{nd}$ December 2011.
**URL:** *http://www.wsc.ec.gc.ca*

Fraser Basin Council (2008). *Flood Hazard Management on the Fraser River*. Accessed 5$^{th}$ December 2011.
**URL:** *www.fraserbasin.bc.ca/programs/flood.htm*

Friedman, J., Hastie, T. and Tibshirani, R. (2001). *The elements of statistical learning*, Vol. 1, Springer Series in Statistics.

González, R. and Woods, R. (2008). *Digital image processing*, Pearson/Prentice Hall.

González, R., Woods, R. and Eddins, S. (2004). *Digital Image processing using MATLAB*, Dorling Kindersley.

Gore, J. A. and Shields, F. D. (1995). Can large rivers be restored?, *BioScience* **45**(3): pp. 142–152.

Graham, D. J., Rollet, A.-J., Piégay, H. and Rice, S. P. (2010). Maximizing the accuracy of image-based surface sediment sampling techniques, *Water Resources Research* **46**(2).

Graham, D., Reid, I. and Rice, S. (2005a). Automated sizing of coarse-grained sediments: image-processing procedures, *Mathematical Geology* **37**(1): 1–28.

Graham, D., Reid, I. and Rice, S. (2005b). A transferable method for the automated grain sizing of river gravels, *Water Resources Research* **41**: W07020.

Green, J. (2003). The precision of sampling grain-size percentiles using the Wolman method, *Earth Surface Processes and Landforms* **28**(9): 979–991.

Hall-Beyer (2007). *Tutorial: GLCM Texture*. Accessed 9$^{th}$ December 2011.
**URL:** *http://www.fp.ucalgary.ca/mhallbey/tutorial.htm*

Ham, D. (2005). *Morphodynamics and sediment transport in a wandering gravel-bed channel: Fraser River, British Columbia*, PhD thesis, Department of Geography, University of British Columbia, Canada.

Ham, D. and Church, M. (2003). *The sediment budget in the gravel reach of the Fraser River*, Department of Geography, University of British Columbia.

Haralick, R. (1979). Statistical and structural approaches to texture, *Proceedings of the Institute of Electrical and Electronics Engineers* **67**(5): 786 – 804.

Haralick, R. M., Shanmugam, K. and Dinstein, I. (1973). Textural features for image classification, *Systems, Man and Cybernetics, Institute of Electrical and Electronics Engineers Transactions on* **3**(6): 610 –621.

Hill, G., Maddock, I. and Bickerton, M. (2008). River habitat mapping: are surface flow type habitats biologically distinct?, *British Hydrological Society 10th National Hydrology Symposium, Exeter* pp. 165–171.

Ibbeken, H. and Schleyer, R. (1986). Photo-sieving: A method for grain-size analysis of coarse-grained, unconsolidated bedding surfaces, *Earth Surface Processes and Landforms* **11**(1): 59–77.

Ierodiaconou, D., Leblanc, M., Laurenson, L., Stagnitti, F. and Versace, V. (2005). Mapping land use in a large agricultural basin: a comparison between classification techniques, *in* C. A. Brebbia and J. S. Antunes Do Carmo (eds), *River basin management III*, Wit Press, Southampton, England, pp. 535–544.

Jensen, J. (2005). *Introductory digital image processing: a remote sensing perspective*, Prentice Hall series in geographic information science, Prentice Hall.

Lane, E. and Carlson, E. (1953). Some factors affecting the stability of canals constructed in coarse granular materials, *Proceedings: Minnesota International Hydraulic Convention*, ASCE, pp. 37–48.

Leopold, L. (1970). An improved method for size distribution of stream bed gravel, *Water Resources Research* **6**(5): 1357–1366.

Lillesand, T., Kiefer, R. and Chipman, J. (2008). *Remote sensing and image interpretation*, John Wiley & Sons.

Marcus, W. A. and Fonstad, M. A. (2008). Optical remote mapping of rivers at sub-meter resolutions and watershed extents, *Earth Surface Processes and Landforms* **33**(1): 4–24.

Marcus, W. A. and Fonstad, M. A. (2010). Remote sensing of rivers: the emergence of a subdiscipline in the river sciences, *Earth Surface Processes and Landforms* **35**(15): 1867–1872.

MathWorks (2012). *MATLAB, version 7.14.0.739 (R2012a)*, The MathWorks Inc., Natick, Massachusetts.

McEwan, I., Sheen, T., Cunningham, G. and Allen, A. (2000). Estimating the size composition of sediment surfaces through image analysis, *Proceedings of the Institution of Civil Engineers. Water, maritime and energy* **142**(4): 189–195.

Nelson, T., Gazey, W. J., Rosenau, M. and English, K. (2004). *Status of white sturgeon in the lower Fraser River: Report on the findings of the Lower Fraser River White Sturgeon Monitoring and Assessment Program 1999-2004.* Report prepared for the Fraser River Sturgeon Conservation Society, Vancouver, BC, by LGL Limited, Crescent Beach, BC.

Otsu, N. (1979). A threshold selection method from gray-level histograms, *Systems, Man and Cybernetics, Institute of Electrical and Electronics Engineers Transactions on* **9**(1): 62 –66.

Pina, P., Lira, C. and M., L. (2011). In-situ computation of granulometries of sedimentary grains - some preliminary results, *Journal of Coastal Research,* Special Edition 64, pp. 1727–1730.

Pontius, R., Boersma, W., Castella, J., Clarke, K., de Nijs, T., Dietzel, C., Duan, Z., Fotsing, E., Goldstein, N., Kok, K. et al. (2008). Comparing the input, output, and validation maps for several models of land change, *The Annals of Regional Science* **42**(1): 11–37.

Pu, J., Paik, D., Meng, X., Roos, J. and Rubin, G. (2011). Shape "break-and-repair" strategy and its application to automated medical image segmentation, *Visualization and Computer Graphics, Institute of Electrical and Electronics Engineers Transactions on* **17**(1): 115 – 124.

Qidwai, U. and Chen, C. (2009). *Digital image processing: an algorithmic approach with MATLAB*, Textbooks in Computing, CRC Press.

Rango, A., Laliberte, A., Herrick, J. E., Winters, C., Havstad, K., Steele, C. and Browning, D. (2009). Unmanned aerial vehicle-based remote sensing for rangeland assessment, monitoring, and management, *Journal of Applied Remote Sensing* **3**(1): 033542–033542–15.

Rempel, L. (2004). *Physical and ecological organization in a large gravel-bed river and response to disturbance*, PhD thesis, Department of Geography, University of British Columbia, Canada.

Rice, S. and Church, M. (1996). Sampling surficial fluvial gravels; the precision of size distribution percentile sediments, *Journal of Sedimentary Research* **66**(3): 654–665.

Rice, S. P. and Church, M. (2010). Grain-size sorting within river bars in relation to downstream fining along a wandering channel, *Sedimentology* **57**(1): 232–251.

Rosenau, M. L. and Angelo, M. (2000). *Sand and gravel management and fish-habitat protection in British Columbia salmon and steelhead streams*, Pacific Fisheries Resource Conservation Council, Background Paper No. 2000/3.

Rosenau, M. L. and Angelo, M. (2005). *Conflicts between agriculture and salmon in the eastern Fraser Valley*, Pacific Fisheries Resource Conservation Council, Background Paper.

Rosenau, M. L. and Angelo, M. (2007). *Saving the Heart of the Fraser: Addressing Human Impacts to the Aquatic Ecosystem of the Fraser River, Hope to Mission, BC*, Pacific Fisheries Resource Conservation Council.

Rubin, D. M. (2004). A simple autocorrelation algorithm for determining grain size from digital images of sediment, *Journal of Sedimentary Research* **74**(1): 160–165.

Sabins, F. (2007). *Remote sensing: principles and interpretation*, Waveland Press.

Scott, W. and Crossman, E. (1985). *Freshwater fishes of Canada*, Bulletin (Fisheries Research Board of Canada), Fisheries Research Board of Canada.

Serra, J. (1982). *Image analysis and mathematical morphology*, London.: Academic Press.[Review by Fensen, EB in: J. Microsc. 131 (1983) 258.] Review article General article, Technique Microscopy Staining, Mathematics, Cell size (PMBD, 185707888).

Soh, L.-K. and Tsatsoulis, C. (1999). Texture analysis of sar sea ice imagery using gray level co-occurrence matrices, *Geoscience and Remote Sensing, Institute of Electrical and Electronics Engineers Transactions on* **37**(2): 780 –795.

Sparks, R. E. (1995). Need for ecosystem management of large rivers and their floodplains, *BioScience* **45**(3): pp. 168–182.

Tockner, K., Paetzold, A., Karaus, U., Claret, C. and Zettel, J. (2006). Ecology of braided rivers, *in* G. Smith, J. Best, C. Bristow and G. Petts (eds), *Braided Rivers: International Association of Sedimentologists Series*, Blackwell, p. 396.

Van Der Sanden, J. and Hoekman, D. (2005). Review of relationships between grey-tone co-occurrence, semivariance, and autocorrelation based image texture analysis approaches, *Canadian Journal of Remote Sensing* **31**(3): 207–213.

Verdú, J. M., Batalla, R. J. and Martínez-Casasnovas, J. A. (2005). High-resolution grain-size characterisation of gravel bars using imagery analysis and geo-statistics, *Geomorphology* **72**(1-4): 73 – 93.

Visser, F. and Wallis, C. (2010). Object-based analysis and multispectral low-altitude remote sensing for low-cost mapping of chalk steam macrophytes, *The International Archives of the Photogrammetry, Remote Sensing and Spatial Information Sciences* **XXXVIII-4/C7**.

Warrick, J. A., Rubin, D. M., Ruggiero, P., Harney, J. N., Draut, A. E. and Buscombe, D. (2009). Cobble cam: grain-size measurements of sand to boulder from digital photographs and autocorrelation analyses, *Earth Surface Processes and Landforms* **34**(13): 1811–1821.

Wolman, M. (1954). A method of sampling coarse river-bed material, *American Geophysical Union, Transactions* **35**(6): 951–956.

Xue, Y. and Yang, S. (2005). Image segmentation using watershed transform and feed-back pulse coupled neural network, *Artificial Neural Networks: Biological Inspirations–ICANN 2005* pp. 531–536.

# 9 Appendices

## 9.1 Appendix 1: Weight to Grain Size Conversions

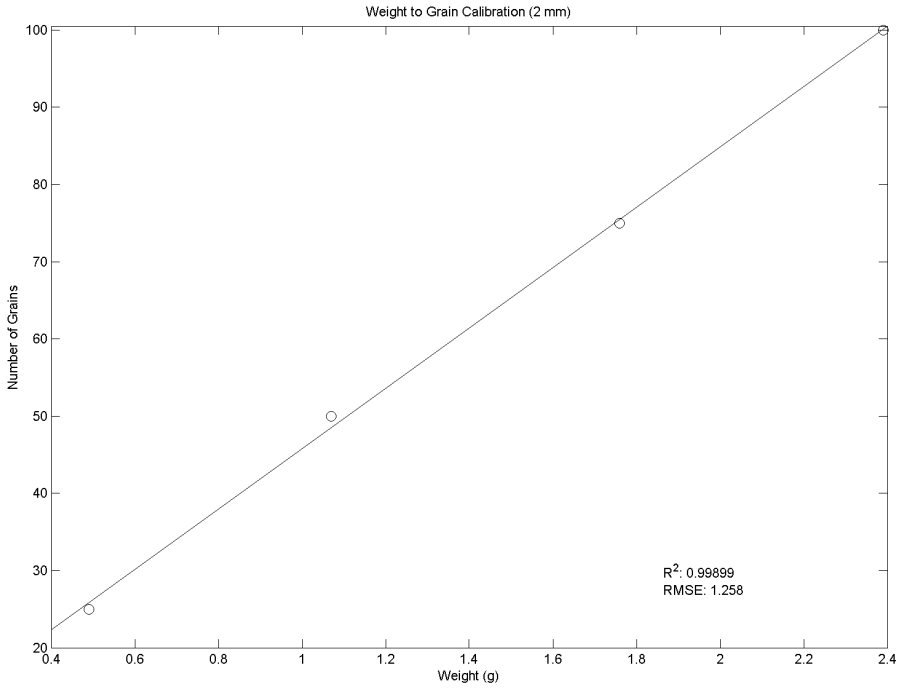


**Figure 19:** *Weight to Grain Size calibration - 2 mm.*

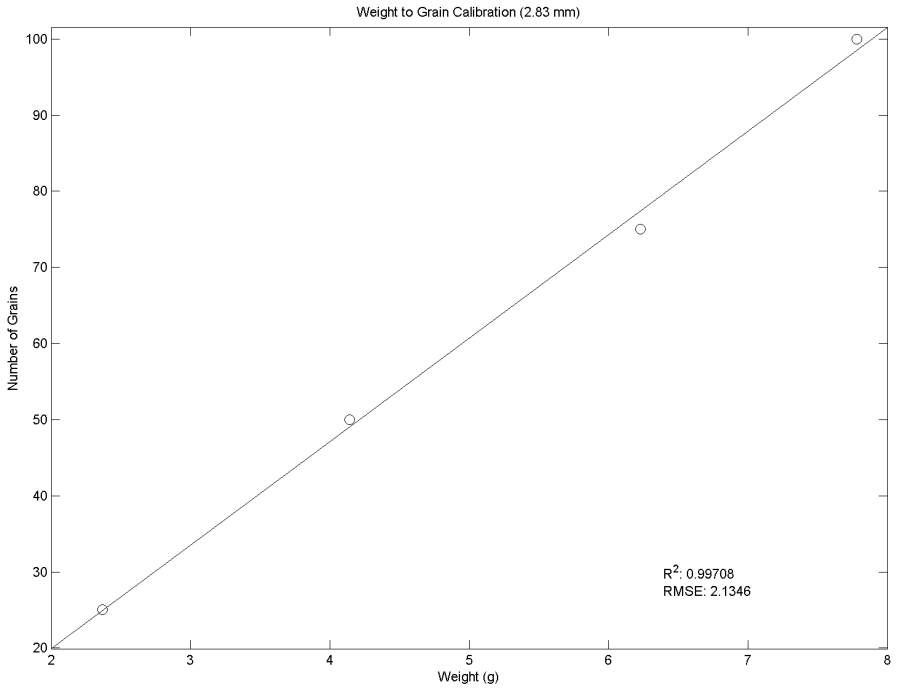


**Figure 20:** *Weight to Grain Size calibration - 2.83 mm.*

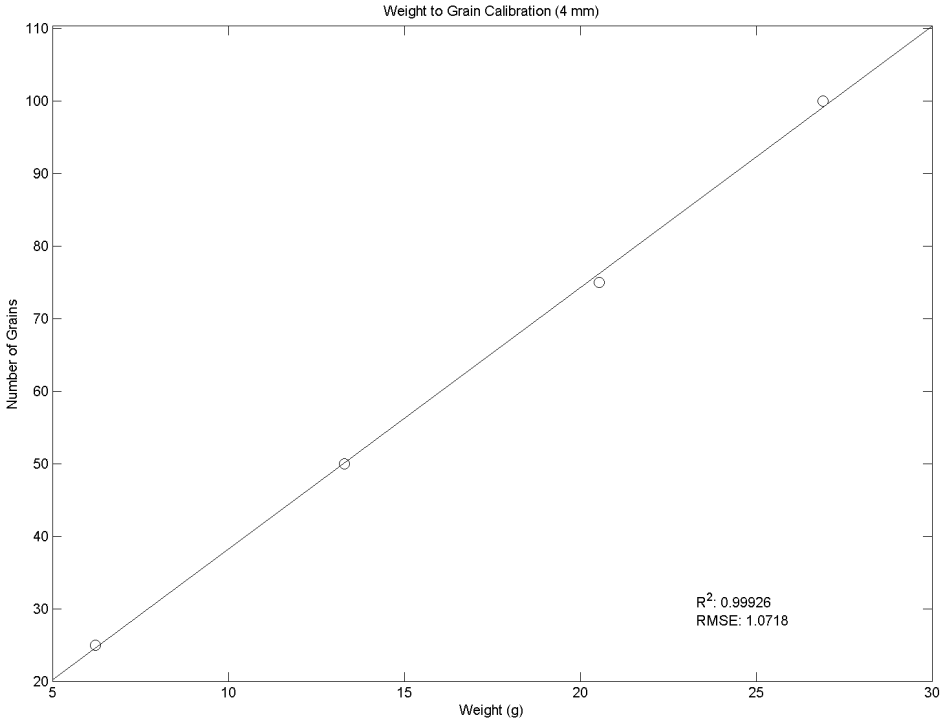


**Figure 21:** *Weight to Grain Size calibration - 4 mm.*

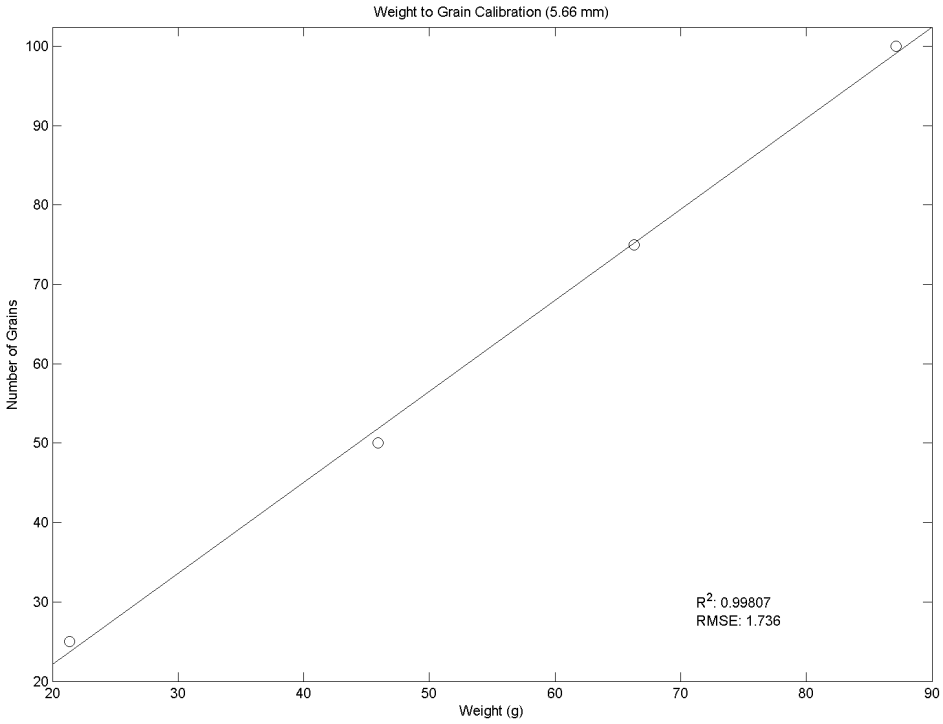


**Figure 22:** *Weight to Grain Size calibration - 5.66 mm.*

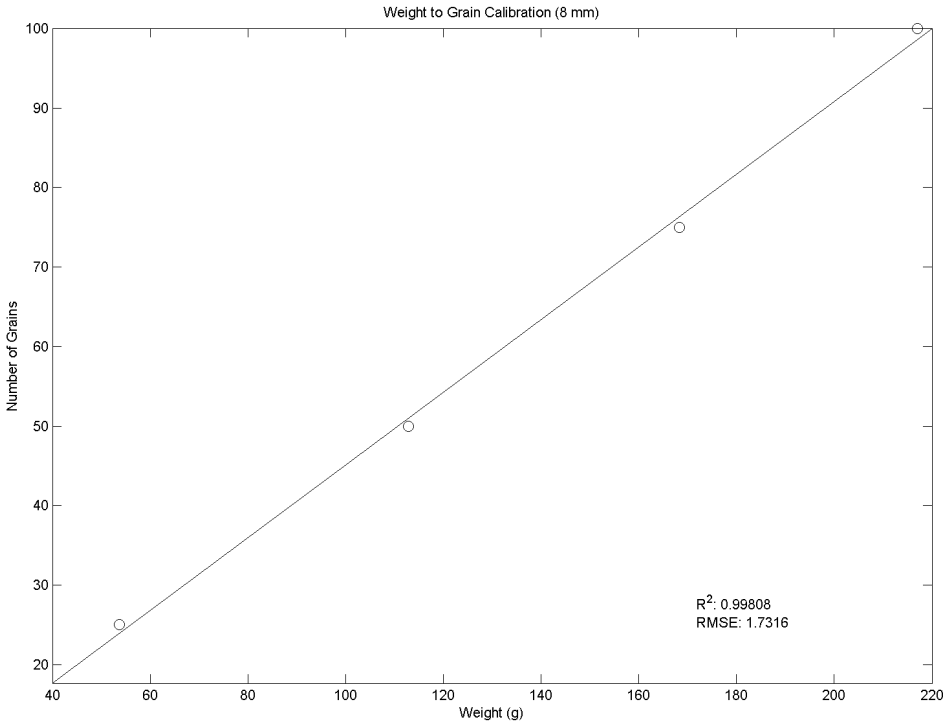


**Figure 23:** *Weight to Grain Size calibration - 8 mm.*

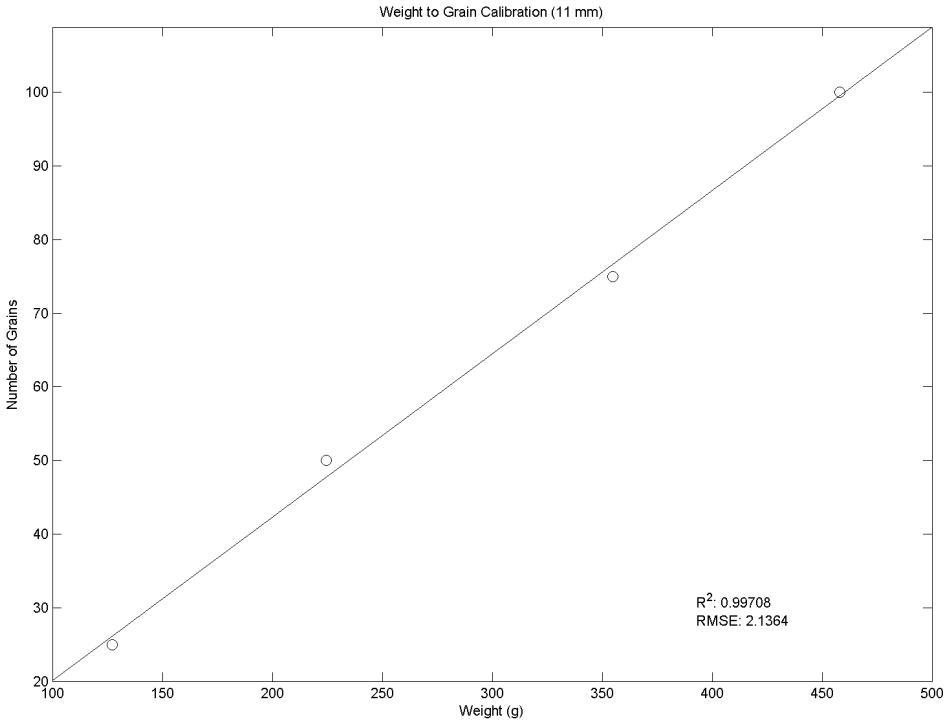


**Figure 24:** *Weight to Grain Size calibration - 11 mm.*

## 9.2 Appendix 2: *Digital Appendix:* Grain Size Maps

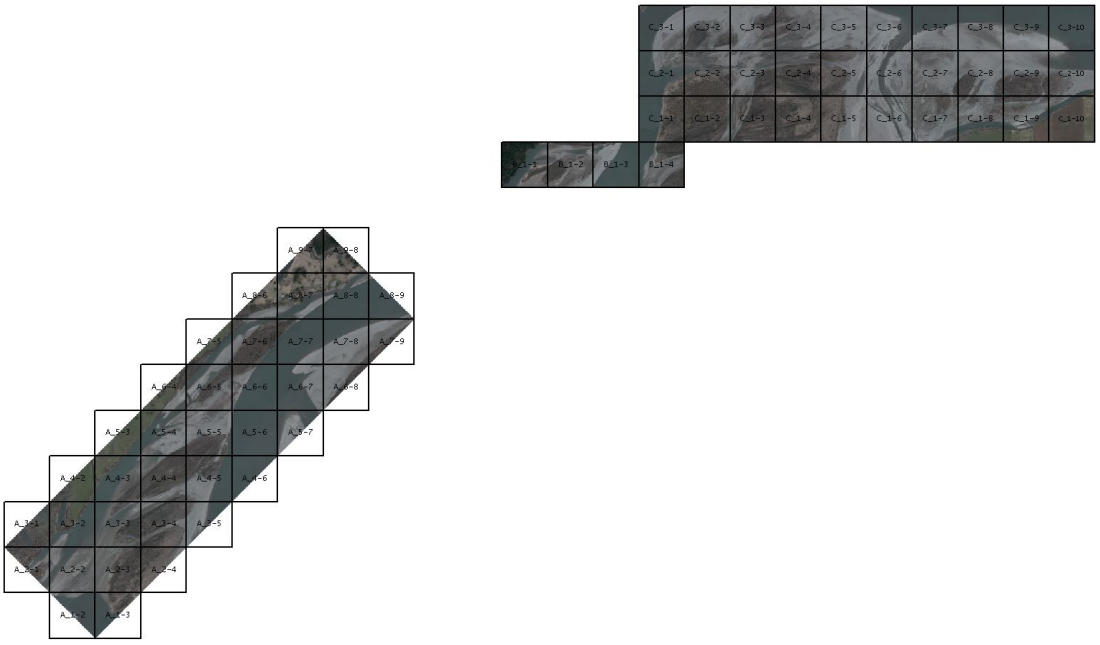

**Figure 25:** *Shows coverage of each of the supplied image tiles.*

For the entire region shown in Figure 8, image tiles were supplied (Section 4.3). Figure 25 shows the layout of the supplied tiles (DTM Mapping Corp., *personal comm.*). Each of these tiles was processed using the optimal parameter set producing 8 additional tiles; binary sand, and percentiles $D_5$ through $D_{95}$. The total size of these files is over 5 GB, with georeferenced images in 16-bit JP2 format. Units are provided in mm×1000 to preserve floating point data (divide by 1000 to return units to mm).

Sample tile A_6-5 is provided at:
`http://www.dur.ac.uk/martin.black/msc`
using the password `gravelbar`.

The full dataset is available on request.